

Gravity modeling of the Alpine lithosphere affected by magmatism based on seismic tomography

Davide Tadiello¹, Carla Braitenberg¹

¹Department of Mathematics and Geosciences, University of Trieste

5 Correspondence to: Davide Tadiello (tadiellodavide@gmail.com), Carla Braitenberg (berg@units.it)

Key words: Gravity modeling, 3D density model, Magmatic underplating, Seismic tomography, AlpsArray

Abstract. The Southern Alpine regions have been affected by several magmatic and volcanic events between the Paleozoic and the Tertiary. This activity undoubtedly has had an important effect on the density distribution and structural setting at lithosphere scale. Here the gravity field has been used to create a 3D lithosphere density model on the base of a high-resolution seismic tomography model. The results of the gravity modeling demonstrate a highly complex density distribution in good agreement with the different geological domains of the Alpine area represented by the European plate, the Adriatic plate and the Tyrrhenian basin. The Adriatic derived terrains (Southalpine and Austroalpine) of the Alps are typically denser (2850 kg m^{-3}), whilst the Alpine zone composed by European terrains provenance (Helvetic and Tauern window) presents lower density values (2750 kg m^{-3}). Inside the Southalpine, south of the Dolomites, a well-known positive gravity anomaly is present and one of the aims of this work was to investigate the source of this anomaly that has not yet been explained. The modelled density suggests that the anomaly is related to two different sources, the first involves the middle-crust below the gravity anomaly and is represented by localized mushroom-shaped bodies interpreted as magmatic intrusions, while a second wider density anomaly affects the lower crust of the Southern Alpine realm and could correspond to a mafic and ultramafic magmatic underplating (gabbros and related cumulates) developed during Paleozoic extension.

20 1 Introduction

In a recent work, Kästle et al. (2018) published a 3D seismic tomography of the lithosphere in the Alps, which forms an ideal basis for a 3D density modeling of the globally available gravity field derived from the integration of satellite and terrestrial data. The 3D inversion of gravity data is an ill-posed problem, since more than one solution exists that reproduces the observations, and therefore constraints from a physical model or from other related disciplines (e.g. seismology, geology, seismics) are necessary. The density model gives an added piece of information to the existing seismic velocity model, as systematic differences in the relation between velocity and density give clues on the petrophysical rock composition as e.g. Bai et al. (2013) and Christensen and Mooney (1995). Moreover, the rheological rock parameters can be defined if both the seismic velocity and density are known. A particular focus of this work is on the lithospheric signatures of the magmatic

activity that affected the Alps from Paleozoic to Paleocene, which conditioned the mechanic characteristic of the crust during the Alpine phase, and in the phases preceding it (Castellarin et al., 2006; Viganò et al., 2013; Zampieri, 1995). The presence of a gravity high located above the Venetian magmatic area comprising the Lessini Mountains, Berici and Euganei hills. (see Fig. 1) has been known for decades (Braitenberg et al., 2013; Ebbing et al., 2006; Zanolli et al., 2006), but an explanation of the high is lacking. The present model shall define the mass sources through a 3D density modeling that starts from the recent seismic tomography with improved spatial resolution (Kästle et al., 2018), acquired in the frame of the Alparray initiative (AlpArray Seismic Network, 2015).



Our 3D density modeling comprises the entire Central and Eastern Alpine arc, and extends down to a depth of 200 km, the same depth of the seismic tomography model. The conversion from seismic velocity to density is done with differentiated approaches, depending on depth and position in upper crust, lower crust or mantle. We used the most recent terrestrial-satellite derived gravity model, and applied the global correction for terrain, which leads to very different Bouguer gravity values compared to the classic local correction up to the 167 km Hayford radius, but is more realistic. The global fields require special attention, because of the far field effect of topography, and we included a dedicated chapter (chapter 3.2) which explains how to deal with this problem, in order to use the fields in the regional density modeling. The Alpine gravity field has been modelled before (Ebbing et al., 2006; Spooner et al., 2019), novel in our study is the use of the Bouguer field corrected for the global topography. A recent study (Spooner et al., 2019) used an approach in which density is constant for lateral crustal domains of typical extension of 80 km to 150 km, and the lithosphere is defined in layers of constant density. The layers have been defined with one layer for unconsolidated and consolidated sediments each, two layers for crystalline crust, one layer for subcrustal lithosphere, and one constant layer for the asthenosphere. In our approach we have not posed any restrictions on the density variability, since we took full advantage of the high resolution seismic tomography model, and emphasis was put to convert the seismic velocities to densities.

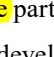
We addressed the central question whether an alteration of the density structure or distribution in the crust and upper mantle below the extended Venetian magmatic Alpine province and the older Athesian magmatism (Bellieni et al., 2010) can be detected. In fact, during magmatic emplacement it can be expected that part of the molten crust is trapped in the lower crust. Only a portion (less than 10 wt%) of the entire molten rocks has erupted to the surface and less than 60 wt% of the whole melt can be emplaced as intrusions in the upper crust (De Min, personal communication). Moreover, this crustal melting is often related to the emplacement of basic mantle derived magma at the Moho discontinuity (magmatic underplating), which provides the necessary temperature to induce a crustal melting.

The working hypothesis is that the above mentioned gravity high could be related to the different magmatic events that have affected the study area at different times, and to the consequent crustal densification and/or juvenile crust formation in underplating.

60 2 Geological introduction

The study area comprises most of the Alpine arc, with particular focus on the magmatism of the southern Alps (Fig. 1). The southern Alpine domain represents the ~~undeformed~~ retro-wedge of an orogeny of double vergence (Dal Piaz et al., 2003; Zanchetta et al., 2012). To the north it is delimited by the dextral Periadriatic line, also known as Insubric line. The South-Alpine terrains formed the passive margin of the Gondwana Paleozoic shelf (Muttoni et al., 2009; Stampfli and Borel, 2002).

65 The central South-Alpine realm  is characterized by three principal fault systems: the Valsugana fault, the Giudicarie fault, and the Schio-Vicenza fault, all active in the late Permian (Viganò et al., 2013). A fault system consists of individual faults, that are under the influence of an over  lying stress field. They move individually, so as to bring the system into equilibrium in response to the applied stress field.

The late Paleozoic-Mesozoic rifting created a system of NS oriented faults, which induced the separation of the Lombardic basin from the Veneto platform, documented by the variable thickness of the Triassic and Cretaceous sediments (Bertotti et al., 1993). From the late Cretaceous to the early Eocene, the extensional regime is inverted due to the convergence between Gondwana and Laurasia, which generates **compressional** systems which initiate to the west of the Giudicarie, and later extend to the eastern Dolomites (Zanchetta et al., 2012). Later, the Giudicarie line is affected by two **compressive** phases: in mid-late Miocene the ENE-WSW oriented thrusts of the Valsugana line develop, which exhum  part of the Hercynian basement. In late 75 Miocene and Pliocene the NE-SW oriented thrusts of Bassano and Grappa-Montello developed, together with reactivation of faults in the Giudicarie (Castellarin et al., 2006; Castellarin and Cantelli, 2000). From end Paleozoic up to Tertiary different magmatic events have affected the South Alpine realm with intrusive and effusive products, that range from basic to acid. According to Castellarin and Cantelli, (2000) the volcanic and magmatic volumes have contributed to considerably increase the **rigidity** of the crust, with implications on the tectonics and geodynamics.

80 2.1 Permian Magmatism

The South Alpine units have been affected by large volumes of magmatism in the Paleozoic (285–260 Ma), with volcanic and plutonic products of acid and basic type (Rottura et al., 1998). The thickness of the deposits has an average value of 900 m, and reaches up to 2000 m (Rottura et al., 1998), and are represented by the ignimbrites and rare flows of the Athesian Volcanic District. These volcanic rocks are bordered by several outcropping granitic intrusions and the whole setting has some 85 similarities with the coeval Ivrea-Verbano system (De Min, personal communication), which has been interpreted as the remnants of a super-volcano (Quick et al., 2009). The units that belong to this age are the porphyritic Athesian platform, intrusions of Cima D'Asta, Bressanone-Chiusa, Ivigna, Monte Croce, Monte Sabion, Monte Luco. These magmatic products indicate important crustal contamination which could be triggered by previous subduction (Variscan?), as indicated by their geochemical properties (Rottura et al., 1998). The magmatism probably has originated in a post-Hercynic phase in a trans- 90 tensive tectonic regime. According to Rottura et al.(1998) the magmatism was generated due to a lithospheric thinning followed by:

- an asthenospheric upwelling,
- consequent partial melting of the asthenospheric mantle due to adiabatic decompression,
- production of gabbro which, stored in underplating, has thermally perturbed the fertile crust,
- consequent production of crustal melts which mixed with more evolved mantle derived magma.

2.2 Triassic Magmatism

The Triassic magmatism affected a continental area which at the time bordered the western Tethys, and comprised the Southalpine, Dinaric, Transdanubian and Austral-alpine domains (Abbas et al., 2018). In the Dolomites the magmatic rocks are rare pyroclastics, dykes, sills, subaerial and marine volcanics, next to intrusives found at Predazzo and at Monti Monzoni.

The origin of the magmatism has been hypothesized as due to a plume, subduction, or extensional events at lithospheric scale (Abbas et al., 2018; Casetta et al., 2018). The magmatism could be associated to activation of regional strike-slip faults during the Ladinian (Abbas et al., 2018). In comparison with the Paleozoic magmatic event, the Triassic magmatic volume appears to be more modest and characterized by a stronger abundance of basic and intermediate products. In the Dolomitic area these intrusions and vulcanites outcrop exactly inside the Permian magmatic structure. According to De Min et al. (2020) this could be related to the presence, in that time, of a depleted crust (depleted during the Paleozoic event) which scarcely interacted with the mantle derived melts stored in underplating. These latter could therefore have evolved without heavily contributing to a crustal fusion. Smaller outcrops of this event are also present along the Valsugana valley and the Recoaro-Pasubio area.

2.3 Tertiary magmatism

From late Paleocene to Oligocene, during 25 Myrs, the terrains south of the Trento platform were affected by a volcanism that extended over an area of 2000 km² (Milani et al., 1999). The principal units form the Lessini mountains, the Berici and the Euganei Hills. The province is characterized by basalts, basanites, transitional basalts and trachytes, which are divided in three categories according to the chemical composition, that ranges from alkaline to tholeiitic. The volcanic activity was due to an extensional regime that accompanied the formation of a foreland basin. The formation is connected to WNW-SSE compression that originated from the Adria-Europe convergence during the Alpine orogeny (Macera et al., 2008; Milani et al., 1999; Zampieri, 1995). During this same period, the calc-alkaline intrusives of Adamello and Mesino-Bragaglia to the west of the southern Giudicarie were emplaced. These batoliths are composed of several intrusive units that formed in Eocene, in an interval between 31 and 35 Ma. Some Rb/Sr datings arrive up to 42 Ma for the location Corno Alto (Martin and Macera, 2014).

3 Geophysical Data

3.1 Seismic tomography database

120 The seismic tomography database from Kästle et al. (2018) was the starting point for the 3D density modeling. This recent model uses seismic stations distributed over the entire Alpine Arc, some stations in part of central Europe and many stations in Italy. The tomography of Kästle et al. (2018) analyses surface waves generated by earthquakes with periods between 8 s up to 250 s and ambient noise observations in a period range of 4 s to 60 s. Given the sensitivity of the seismic periods, the surface waves resolve the deep structures, the ambient noise records the crustal structure and sedimentary basins, with an overlap of

125 the two records for periods between 10 s and 35 s. The tomography inversion included the global dataset of phase-velocity measurements of Ekström (2011) which had been used to constrain the long-period velocity field. The checkerboard test showed that the Alps and Italy are well resolved, except for the French territory, the Adriatic and Tyrrhenian seas. The Dinarides and Pannonian basin belong to the areas with less resolution. Some problems exist also in the resolution of superficial structures in the eastern Po-basin, due to scarce availability of seismic stations. The model resolves the upper mantle well in

130 the Alpine foreland of the Adria plate, of central Europe, of the Pannonian basin and the Ligurian Sea, with reduced resolution below the Alpine region. The model reports shear (V_s) velocities with a grid spacing in latitude of 0.1° , in longitude of 0.146° , and a vertical grid interval of 100 m for the upper 600 m, of 500 m between 1 km and 2.5 km, of 1 km between 3 km and 12 km, of 2 km between 14 km and 84 km, and 5 km between 85 km and 200 km. The present study selects a portion of the model limited to longitudes $8 - 14^\circ$ and latitudes $43 - 49^\circ$.

135 3.2 Gravity field and topographic reduction

The gravity data were calculated from the global gravity model EIGEN6c4 (European Improved Gravity model of the Earth by new techniques (Förste et al., 2014a). The model combines observations from different geodetic satellites, as LAGEOS-1/2 SLR, GRACE GPS-SST, GOCE and incorporates existing models from terrestrial data for the high frequency part. It uses the DTU 2'x2' global gravity anomaly grid from satellite altimetry (Andersen, 2010; Andersen et al., 2010) over the oceans and

140 the EGM2008 model (Pavlis et al., 2012) over the continents. The model is parameterized in terms of a table of spherical harmonic coefficients complete up to degree and order 2190. For degrees above $N=235$ in continental areas, the model reproduces the field of EGM08, over oceanic areas the model DTU12. The choice of the upper degree is justified by the fact that the authors of the model consider this maximum degree as adequate, and statistical evaluations have been made by the authors up to this degree (Förste et al., 2014b)

145 It is customary to reduce the gravity field for the gravity effect of topography, which is available in terms of spherical harmonic expansion, as the model of Hirt et al. (2015) and Hirt and Rexer (2015). The layers describing the topography have been divided into glaciers, oceans, lakes and solid crust, with their respective homogeneous densities equal to 917 kg m^{-3} , 1000 kg m^{-3} , 1030 kg m^{-3} , 2670 kg m^{-3} . We have used the particular model `dv_ELL_RET2014PLUSGRS80`, which includes the gravity of the ellipsoid. We refer to Rexer et al. (2016) for details on how the model was obtained.

150 Due to the fact that several options exist in how to define the functional of the gravity value from the spherical harmonic models of the earth gravity and the topographic effect, we briefly give here the fundamental definitions. Further details can be found for instance in the textbooks Torge (2011), Torge and Müller (2012) and Barthelmes (2013).

The Bouguer anomaly is defined as:

$$g_{bg} = g_{fa} - g^T \quad (1)$$

155 Here the gravity effect of the topography (g^T) is subtracted from the free-air anomaly (g_{fa}). The Free air anomaly according to Molodensky (Torge, 2011) is defined as:

$$\Delta g_{fa} = g(P) - \gamma(Q) \quad (2)$$

with $g(P)$ the observed value in point P, and $\gamma(Q)$ is the gravity value of the reference ellipsoid calculated at the height of the telluroid. The gravity disturbance is defined as:

160
$$\delta g_{fa} = g(P) - \gamma(P) \quad (3)$$

Here the gravity field of the ellipsoid is subtracted from the observed gravity field, both calculated in the observation point P. The gravity anomaly and gravity disturbance are related to the disturbing potential T ($T(P) = W(P) - U(Q)$) as follows:

$$\delta g_{fa} \approx -\frac{\partial(W-U)}{\partial h} \quad (4)$$

$$\Delta g_{fa} \approx \delta g_{fa} - 2h^{-1}(W - U) \quad (5)$$

165 Here W is the earth gravity potential and U is the potential of the ellipsoid, and h is the geometric height. Vaníček et al. (2004) show that due to the second term which enters the definition of the gravity anomaly, the gravity disturbance must be used when deriving the gravity potential of the topography for the Bouguer correction. In fact, otherwise the second term of Eq. (5) would be applied twice. In spectral domain the derivatives translate to the following:

$$\Delta g_{fa}(r, \lambda, \varphi) = \frac{GM}{r^2} + \sum_{n=0}^N \left(\frac{R}{r}\right)^n (n-1) \sum_{m=0}^n (C_{nm}^T \cos m\lambda + S_{nm}^T \sin m\lambda) P_{nm}(\sin \varphi) \quad (6)$$

170
$$\delta g_{fa}(r, \lambda, \varphi) = \frac{GM}{r^2} + \sum_{n=0}^N \left(\frac{R}{r}\right)^n (n+1) \sum_{m=0}^n (C_{nm}^T \cos m\lambda + S_{nm}^T \sin m\lambda) P_{nm}(\sin \varphi) \quad (7)$$

where C_{nm}^T and S_{nm}^T are the Stokes coefficients of the gravity potential of either earth or topography, from which the Stokes coefficients of the ellipsoid have been subtracted. G is the gravitational constant, M is the Earth mass, n, m are the degree and order of the spherical harmonic expansion, N is the maximum degree of the expansion, and r, λ, φ are the three spherical coordinates radius, longitude and latitude. The calculated gravity anomaly and disturbance are shown in Fig. 2, and it is seen that the gravity disturbance is systematically higher than the gravity anomaly, confirming Vaníček et al. (2004).

Subtracting the gravity effect of topography g^T calculated with the model RET2014 (Rexer et al., 2016) and shown in Fig. 3b from the gravity disturbance derived from EIGEN6c4, the “Bouguer gravity disturbance” (Tenzer et al., 2019) (Fig. 3c) is obtained. This Bouguer field corresponds to the classical complete Bouguer anomaly, that includes both the topographic

correction on top of the Bouguer plate correction, with the difference that we consider the entire Earth, and do not limit the topographic corrections to the Hayford radius of 167 km. We fulfilled all calculations (Barthelmes, 2013) with the publicly available gravity calculation service of ICGEM (International Center for Global Gravity Field Models; www.icgem.com). The 3D density modeling we intended to fulfil was made on a window of less than 6° degrees latitude by 6° degrees in longitude, and a maximum depth of 200 km. The limit in lateral and depth extension of the model produces a bandlimited gravity field that can be modelled. It is therefore necessary to reduce the lowest degrees of the gravity field of topography, since they introduce a field which is due to distant masses and are uncorrelated to the regional properties of the gravity field which was modelled in the present study. We found that starting with degree and order $N > 10$ the field of topography starts resembling the regional topography, and used this value as lower limit for the spherical harmonic expansion of the fields. This value agrees with the findings of Steinberger et al., (2010), who define degree 10 the limit of lithospheric contributions, lower degrees having their origin in the deep mantle or lower. The non-band-limited Bouguer field (Fig. 3a), the non-band-limited effect of topography (Fig. 3b) and the band-limited Bouguer field (Fig. 3c) are displayed in the respective maps. The band-limited Bouguer map (Fig. 3c) obtained for degrees $10 < N \leq 2190$ (EIGEN 6c4 and RET2014) has the same features as the non-band-limited map (Fig. 3a), with the difference that now the bounds of the Bouguer anomalies are more similar to those of the regional topographic reduction obtained with the Hayford radius (e.g. Braitenberg et al., 2013; Ebbing et al., 2006; Spooner et al., 2019; Zanolla et al., 2006). In fact, the band-limited Bouguer disturbance is -160 mGal below the Alps, and -130 mGal below the Appennines, against the non-band-limited Bouguer values of -60 mGal over the Alpine arc. Another area with clear negative values is close to the front of the Tuscan-Emilian Appennines, presumably due to the combined effect of sediments of the Po plain and the crustal thickening due to stacking of sediment layers of the Appennines. The markedly different values obtained with the global reduction are inherent to the distant masses that are neglected in the regional reduction, but which are largely compensated by the isostatic crustal thickness variations (Szwilius et al., 2016). In the following we used the band-limited Bouguer disturbances (Fig. 3c).

4 Method

The aim of this work was to develop a three-dimensional density model of the Alpine region constrained by seismic tomography. The method was developed in four steps:

- Moho discontinuity investigation;
- Seismic wave velocity-density conversion for mantle and crustal layers;
- Gravimetric forward modeling and comparison between modelled results and the observed gravity data;
- Inversion of the gravimetric residual and model density correction

4.1 Moho discontinuity depth definition

The Moho discontinuity depth was defined by studying the vertical variation of the tomographic seismic velocity from Kästle et al. (2018). First of all, a preliminary velocity field analysis was fulfilled using other Moho models proposed by a) Tesaro et al. (2008) (EuCrust07), b) Laske et al. (2013) (Crust1.0), and c) Grad et al. (2009) (MohoGrad). From this field analysis we discovered that the mean S-wave velocity of the crust-mantle transition is 4.1 km s^{-1} with a standard deviation of 0.2 km s^{-1} (Table 1). This velocity value is in agreement with the velocity change at Moho between 3.85 km s^{-1} and 4.48 km s^{-1} proposed in the 1D global model AK135 (Kennett et al., 1995). Therefore, on the basis of this statistics, a preliminary result was obtained researching the maximum vertical gradient of the velocity profile, within a velocity range between 3.8 km s^{-1} and 4.4 km s^{-1} , that represents the mean value plus and minus one standard deviation. To improve the stability and the reliability of this approach, another condition was imposed on the velocity surrounding the Moho surface obtained from the maximum gradient analysis. The S-wave velocity reported 4 km above and below the Moho surface had to be respectively smaller and larger than the typical velocity of the lower crust and uppermost mantle. The mean P-wave velocity of the European lower crust was estimated to about 6.5 km s^{-1} , while in the upper mantle, the P-wave velocity of the peridotite was larger than 8 km s^{-1} (Christensen and Mooney, 1995). From this observation, the limits for the P-wave velocity above and below the Moho have been assigned to be of 6.8 km s^{-1} and 7.4 km s^{-1} .

The results show a good agreement with the Moho models proposed by the other authors (Fig. 4). Some differences are represented by an important crustal thickening located in the Ivrea-Verbano (D1) area and below the Istrian region (D2). Also the geometry and the depth found for the two main orogens (D3) are significantly different from the reference models, and our model seems to have a better resolution.

4.2 Seismic wave velocity to density conversion for mantle and crustal layers

The Moho discontinuity allowed to divide the entire tomographic volume in crustal and mantle layers. For each layer, a different approach and relations were used, to define the density values starting from the tomographic seismic velocity.

4.2.1 Crustal conversion

A huge set of relations have been proposed by different authors to convert the seismic wave velocity to density (Brocher, 2005) and most of these equations principally transform the compressional wave velocity (V_p) to density. For this reason, it was necessary to convert the tomographic V_s in V_p through the “Brocher’s regression fit” (Brocher, 2005), a relation obtained from seismic, borehole and laboratory data for different kinds of lithology and valid for V_s between 0 and 4.5 km s^{-1} . Given the extreme variability of the crustal rocks present in the study area, a density estimation was carried out through two equations: the “Gardner’s rule” by Gardner et al. (1974) and the “Linear regression fit” proposed by Christensen and Mooney (1995). The first is an empirically derived equation that relates seismic P-wave-velocity to the bulk density of the lithology. It is very popular in petroleum exploration because it can provide information about the sedimentary lithology from interval velocities

obtained from seismic data. On the other hand, Christensen and Mooney (1995) proposed a widely used linear density-Vp relation for crystalline rocks obtained from seismic refraction and laboratory data, in order to define the continental crust features as a function of the different geodynamic context. In our work, the sedimentary rocks velocity domain was distinguished from the crystalline domain by the velocity value at which the two curves intersect, as seen in Fig. 5 and also in Brocher (2005). For the sedimentary rocks Gardner's rule was used, for the crystalline rocks the linear fits of Christensen and Mooney (1995) were used, which are given for depth ranges from 10 km to 50 km. The intersection velocity is dependent on depth, for the shallower depths of 10 km for instance, the velocity is $V_p = 6 \text{ km s}^{-1}$, at 50 km the intersection is at $V_p = 5.2 \text{ km s}^{-1}$ (see Fig. 5). The red symbols in Fig. 5 show the distribution of the final density values in the graph, and will be discussed later. A mistake in the calculation of the density is made, when the fit of Christensen and Mooney is used for sedimentary rocks, and Gardner's rule is applied for crystalline rocks. This miscalculation is though limited, if we analyse the velocities of sedimentary rocks and crystalline rocks. Due to the steeper slope of the relation of Christensen and Mooney, the resulting density is higher compared to Gardner's rule at the same velocity. For sedimentary rocks, limited to the upper crust, the only rocks that would have an overestimated density would be dolomite, since the other sedimentary rocks generally have velocity below 6 km/sec. For the crystalline rocks, there are limited rocks that have a velocity below 6 km/sec and are in danger of overestimating their density, by switching to Gardner's curve. For instance, only Quartzites, Andesites, Meta-Grauwacke, Serpentinites are in danger to be misplaced (Mooney, 2007).

255

4.2.2 Mantle conversion

A different approach was used for the velocity conversion in the upper-most mantle; in this case, the tomographic velocity model was compared to a Synthetic Upper Mantle model (SUM). The SUM was modelled through the open-source software Perple_X (Connolly, 2005), which allows the computation and mapping of the phase equilibria, rheological properties and density.

For this modeling the TECTON bulk rock composition model (Griffin et al., 2009) of the mantle was used, which represents an estimate of the mean composition of a Neoproterozoic-Phanerozoic Sub-Continental Lithospheric Mantle (SCLM), gained from xenolith suites and peridotite massifs data. In Table A-1, the major elements of the TECTON composition are shown, of which we used the most abundant elements, up to a total content of 98.9 %, leaving out the minor elements with percentages less than 1 %. The software calculates the stable phases for a two-dimensional grid of temperature (T) and pressure (P) conditions, typical for the mantle up to a depth of 200 km ($T_{\min} = 350 \text{ }^{\circ}\text{C}$ to $T_{\max} = 1600 \text{ }^{\circ}\text{C}$, $P_{\min} = 0.1 \text{ GPa}$ to $P_{\max} = 7 \text{ GPa}$). The software requires setting some calculation parameters, which are defined here. The thermodynamic model is the Holland and Powell (1998) model, which is the default. For the computation of the phase equilibria and the elastic properties, the default parameters were used. Further options included: no presence of saturated fluids, calculation with saturated components not present, chemical potentials, activities and fugacities are not independent variables. The adopted mineral phases for the synthetic mantle SUM are: Olivine, Clinopyroxenes, Orthopyroxenes, Garnet, Spinel and Plagioclase and the

thermodynamic model for these solid solutions is again the Holland and Powell (1998) database. We refer to the documentation of the software and the original paper for the thermodynamic modeling details, which are out of scope of the present work.

The result consists in the equilibrium phase diagram, which shows the fields of stability of different equilibrium mineral assemblages for the adopted bulk-rock composition, depending on the P-T combinations. For each assemblage a number of parameters are given as well, from which we select Vs and density, shown in Fig. 6.

The conversion of the seismic velocity to density was made comparing the tomographic velocity at its given depth, with the synthetic velocity at the pressure corresponding to the depth. The pressure was calculated integrating the lithospheric density column from top to the corresponding depth. From the topography to the bottom of the crust, the crustal density model calculated from the crustal seismic velocities was used. The resulting pressure at the base of the crust was used for converting the seismic velocity to density in the resolution cell below the Moho, and then iteratively downwards to the base of the model. The temperature was left unconstrained and corresponds to the value that allows to match the tomographic and synthetic velocity at the given pressure. The above described density values define the starting model which is corrected through the gravity inversion discussed in the next chapters.

4.3 Gravimetric forward modeling and comparison between modelled results and the observed gravity data

In the previous section the transformation of P-wave velocities to density values was described. The next step was to discretize the entire model with tesseroids, mass elements defined in spherical geocentric coordinates (Anderson, 1976; Grombein et al., 2013; Heck and Seitz, 2007; Wild-Pfeiffer, 2008). This task was done building these elements as function of the original three-dimensional tomographic grid, from which we defined the density value of the tesseroids. In order to make the modelled gravity effect comparable with the observed gravity anomaly, the obtained density model was reduced by the reference density model PREM (“Preliminary Reference Earth model”). This reference model represents the mean physical features of the earth, including elastic parameters, seismic attenuation, density, pressure and the earth-radius dependent gravitational value in function of radius. Being a global model, it was modified in order to obtain a dimensional model comparable with a continental crust, eliminating the first 3 km of seawater and lowering the Moho depth. All changes to the original PREM model were done to maintain the pressure value at the base of the model constant and we call this modified model co-PREM (Fig. A1 in Appendix). Applying the co-PREM model is equivalent to subtracting a constant value from the modelled gravity values, since gravity has a linear relation to density. For the crustal model a different choice of the reference model will not alter the results, because the constant gravity value will be absorbed in the mantle gravity residual field. Therefore, it could give some effect on the density variations in the mantle. Assuming a difference in the gravity field of the reference model of 10 mGal or 50 mGal, there would be an upward bias in the mantle densities of about 8 kg m^{-3} or 40 kg m^{-3} , a very small value compared with the mantle densities of close to 3400 kg m^{-3} .

Figure 7a shows the result of the gravitational forward modeling, developed through the software Tesseroids (Uieda et al., 2016). The gravity anomaly map presents two well defined negative anomalies induced by the crustal thickening below the orogens and the extensive positive anomaly produced by the Tyrrhenian crust. At large scale, the modelled anomaly reproduces

305 in broad outline the observed data (Fig. 3c) and from the difference between observed-modelled anomalies, we obtained the residual gravity map (Fig. 7b). The residual map shows that the modelled anomaly differs from the observed map by values that range from -40 mGal to $+220$ mGal. Furthermore, the residual outlines three regions characterized by different trends: Germany and part of Switzerland is characterized by negative values reaching peaks around -40 mGal (A1), the Tyrrhenian basin shows a positive residual around $+80$ mGal (A2), while the residuals are generally positive in all of the remainder study
310 area, reaching values of $+200$ mGal (A3).

4.4 Inversion of the gravimetric residual and model density correction

Theoretically, the gravity residual map represents the extent to which the starting density model diverges from the one of the infinite possible density distributions that produced the measured gravity anomaly. In order to improve the reliability of the starting density model an inversion algorithm was developed based on the residual between observed and modelled data. As
315 seen in Fig. 8, the first step is to separate the long wavelength residual component from the short wavelengths, and to estimate the different contributions of the mass sources that generate the residual signal.

The distinction between crustal and mantle contribution, which corresponds to the long and short wavelengths respectively, has been done by fitting a third-order polynomial surface to the values of the residual map (Fig. 9), and the choice of the order was made by a qualitative evaluation depending on the features and the large scale trend of the residual anomaly map.
320 Starting with degree zero, up to degree three, the long wavelength signal is uncorrelated to both topography and geology, and was assigned to the mantle component. Starting with degrees higher than 3 the polynomial started to show smaller scale features which correlated with the geometrical and physical properties of the crust. We therefore think that the third order polynomial is qualitatively the correct choice to separate the mantle from the crustal component. The mantle component has a long period trend oriented NW–SE. The third order polynomial allows to separate this very long-wavelength signal from the
325 crustal contribution. Considering the changes in absolute gravity values, we observe that after subtracting the first model obtained from the seismic data, the values had been reduced from the starting range of 360 mGal to a range of 270 mGal (Fig. 7). The biggest large scale anomalies had been largely reduced, leaving a residual field that is dominated by smaller scale gravity anomalies. Separating the mantle contribution from the crustal contribution shows that the high amplitude of the residual comes from the mantle (Fig. 9a), with a range of 270 mGal, whereas the crustal contribution is mostly limited to a
330 range of 140 mGal (Fig. 9b) with very located small scale features reaching to a range of 190 mGal.

Then, once we obtained the two components, the algorithm provided the “linear iterative inversion” section, in which a rough first density correction was computed with the “Infinite slabs gravimetric effect” equation:

$$\Delta\rho = \frac{\Delta g}{2\pi GH} \quad (8)$$

335 where $\Delta\rho$ is the density correction, Δg is the short or long gravimetric residual component, H represents the thickness of the considered layer (crustal or mantle layer) and G is the gravitational constant. Then the density correction was applied to the starting density model, the vertical distribution of the total mass correction was assigned through the following equation:

$$\rho_{i_{new}}(z) = \rho_{i_{old}}(z) + \Delta\rho_n H_n \left(\frac{\rho_{i_{old}}(z)}{\sum_{i=1}^N \rho_{i_{old}}(z) \Delta z_i} \right) \quad (9)$$

340 where $\rho_{i_{new}}$ and $\rho_{i_{old}}$ are respectively the new and the old density values, $\Delta\rho_n$ is the density correction, H_n is the height of the considered layer (crust or mantle layer) and Δz_i represents the height of the mass element belonging to the single density profile. We applied the density correction, obtained a new mass distribution, and computed the forward modeling of the corrected density model in the next step. The results of the latter operation was compared with the observed data producing, for each iteration, a new gravimetric residual map. The density was free to vary at the stage of the iterations inside the bounds of acceptable densities in crust and mantle, defined from laboratory measurements. These are as follows: density in crust: 2200
345 kg m⁻³ to 3000 kg m⁻³; mantle: 3000 kg m⁻³ to 3500 kg m⁻³. The iteration was stopped when the root mean square residual reached the value below 3 mGal. The number of iterations needed were 6 for the crust, and 5 for the mantle. This algorithm allowed to define the density correction, which was applied to the three-dimensional starting model and allowed to compare the gravity effect of this new mass distribution with the observed data. The root mean square density correction over the volume of crust and mantle and the root mean square decrease of the gravity residual, during iterations are shown in Fig. 10. It can be
350 seen how the gravity residual quickly decays in the first iterations, and then remains close to constant when reaching the level of 3 mGal. The final density values in relation to the Vp velocity are shown in Fig.5, as red symbols. It can be seen that the final density values are inside the root mean square experimental deviations from the theoretical relations between density and velocity, and are therefore physically acceptable. The map of the final total crustal density corrections, corresponding to the sum of the corrections calculated in each of the six iterations and the final gravity residual, are displayed in Fig. 11 a,b.
355 Several error sources intrinsically affect the final 3D density model. A forward error propagation is very difficult to be performed, because quantitative estimates of all errors, starting from the seismic model are not available to us. Therefore, it is hard to provide a quantitative error estimation of the final density model. However, some general aspects can be considered to understand which are the main sources of uncertainty and their effect during the modelling process. First of all, Moho discontinuity definition has a larger impact for the mid-long component of the gravimetric field and uncertainty of some
360 kilometres of this surface can produce several mGal of gravity variation, significantly changing the modelled anomaly. Analysing the proposed method, another set of critical error sources are the different equations used for the P-wave velocity-density transformation. The proposed equation reflected regional studies based on different input data acquired from different geological contexts. Other error sources are the uncertainties affecting the tomographic velocity model used as input data for this study and the linear inversion algorithm based on the simple Bouguer plate correction. Apart from the mentioned
365 uncertainties, we estimate the amount of correction on the crustal density model after the final iteration of the inversion and use this as a quantification of the uncertainty. For the crustal column, we obtain a root mean square value of the final correction of up to 2 kg m⁻³, shown in Fig. 11c. The final gravity residual has a root mean square value of less than 2.7 mGal.

5 Results

5.1 Alpine region density distribution

Figure 12 shows horizontal slices of the final density model at increasing depths ranging between 5 km and 40 km. Here we describe the main features.

In the first kilometres, up to 15 km depth (Fig. 12 a,b,c), the low density values are due to the two main sedimentary basins situated in the fore-deeps of Alps and Apennines. In the European plate, the Molasse basin is trending in W–E direction along the northern Alps front (LMB), and this sedimentary layer is wider and thinner in the western part whilst it becomes more elongated and thickens in the eastern Bavarian part. In the Adriatic plate, the Po basin (PBL) is characterized by a thicker and less dense sedimentary layer than the Molasse basin. The Molasse basin is shallower (average thickness 5 km, maximum thickness 9 km), than the Po basin (average thickness 9 km, maximum thickness 13 km). As shown in Fig. 12a and 12 b, both modelled basins show a progressive decrease of the densities towards the eastern part of the sedimentary layer (especially at the south of the Po river mouth).

Remaining in the first 15 kilometres, a homogenous density region (2650–2750 kg m⁻³) features the Alpine orogenic upper crust. Inside this domain a relative low-density anomaly (2650 kg m⁻³), corresponding to the Helvetic nappe (HL) and the Tauern window (TWL) is present, while in the Ivrea-Verbano (IVH) zone the density reaches the typical values of the lower crust (2850–2900 kg m⁻³).

Between 15 and 20km (Fig. 12c and 12d) the modelled density represents the gradual transition from upper to lower crust, except in the Tyrrhenian basin (TBH), where the high density values indicate the crust-mantle transition, in agreement with the Moho depths of Fig 4d. In this depth-interval, the Adriatic crust is denser than the European crust; furthermore, a W–E trending high-density ridge (RH) (2900 kg m⁻³) follows the western South-Alpine domains, passing near the Schio-Vicenza fault up to the buried front of the Apennines. As previously seen in the first kilometres, a relative low density domain remains below the Helvetic terrain (HL) and the Tauern window (TWL); a further lower density patch is present in the Adriatic Sea, below the northern Apennines (PBL), and facing the Valsugana thrust system (BBL).

Figures 12e and 12f show the lower crustal modelled density of the European and Adriatic plates, where the relatively low-density values characterising the lower crust of the inner part of the Alpine and Apennine orogens (2800–2850 kg m⁻³) are visible (IPL), while in the outer parts of the two orogens and in the foredeep regions (OPH), the average density is higher (2900–2950 kg m⁻³). Very high values affect the lower crust of the north-western part of the study area, close to the Upper Rhine graben system (GSH) and, furthermore, the W–E trending high-density ridge is still present (RH), reaching higher values at this depth (up to 3000 kg m⁻³ below the Giudicarie and Schio-Vicenza fault system). At 30 km depth, mantle density is present in the Northern European plate and Adriatic Sea, in agreement with the Moho depths of Fig 4d.

At greater depth (Fig. 12g and 12h), the modelled density features of the Alps and Apennines crustal roots and the inner part (LIP) of the two belts are characterized by lower densities ($2800\text{--}2850\text{ kg m}^{-3}$) than the surroundings. Below the orogen's crustal roots, the mantle is marked by a density average value around 3300 kg m^{-3} .

We have computed also the weighted average density for the crustal layer (Fig. 13). The average density distribution reproduces and synthesizes all the features seen above. In the European plate, different domains are present for the area close to the Upper Rhine Graben (GSH) (high-density $2860\text{--}2900\text{ kg m}^{-3}$) and the Molasse basin (MBL) ($2740\text{--}2800\text{ kg m}^{-3}$). Also, the Alps show a density zonation in good agreement with the surface geology: Helvetic terrain (HL) and Tauern window (TWL) are on average less dense than the Penninic (PH), Austroalpine (AH) and Southalpine (SH) nappes. The Adriatic domain is represented by a highly complex density distribution with a heterogeneous low-density area highlighting the Po basin (PBL), the adjacent Adriatic and other two more restricted areas situated in the Piedmont (PDL) and Belluno basins (BBL) regions. In the Apennines, the density values follow the main structural lines defined by the stack of NE to E verging thrust fronts and the back-arc basin affected by extensional tectonics. In the South Alpine domain, the model generally shows high-density values, especially in the Ivrea-Verbano complex (IVH) (3000 kg m^{-3}) and at the Valsugana thrust system (SH) (2870 kg m^{-3}) in the eastern part. The previously discussed W–E high-density ridge which develops from the Ivrea-Verbano anomaly to Schio-Vicenza fault system (RH), and that affects the Trento platform, is also seen in the average crustal density map.

415

5.2 Modelled density in the Venetian gravity anomaly area

Three representative transects across the main gravity anomaly structures of the central-eastern Southern Alps are illustrated in Fig. 14, and discussed in the following.

The A section (Fig. 14) shows the density distribution along the main direction of the Venetian Gravity Anomaly, parallel to the Schio-Vicenza fault. The low density in the southern part of the profile, represents the sediment layer that reaches a thickness of around 13 km in the deepest part (longitude 12.5° E in the profile). As seen before, between the South-Giudicarie fault (SGF) and the buried Apennines thrust front, there is again the increased density area (RH) situated between 25 km and the Moho discontinuity, and extending between 10.8° E and 11.8° E , with a density of $2900\text{--}3000\text{ kg m}^{-3}$. This increased density in the lower crust can be recognized for instance by an upward shift of the 2900 kg m^{-3} isoline, distancing it from the Moho. In the middle crust, two limited mushroom-shaped bodies are lying between 10 and 25 km, the first (MB1) is located below the Venetian Volcanic Province (VVP) and above the high-density plateau (RH) close to latitude 11.5° N , while the second (MB2) is situated below an area between the south Giudicarie fault (SGF) and the Periadriatic Line (PL), corresponding to the outcropping Adamello batholith (AB). Although outside our focus area, we mention a density high along profile A which is located NW of the Periadriatic Line (PL) and affects depths of 30 to 10 km. Along profile A it is located at longitude 9.8° approximately. The recent work of Rosenberg and Kissling (2013) interprets the crustal velocity variations, and notices the

430

upwelling of the velocity lines north of the Periadriatic Line, with a lower effect in the Central Alps, and an increase of the effect towards the Central-Western Alps. They interpret it as lower crustal accreted terrain which is deformed and brought to upper crustal levels north of the Periadriatic line. From our modeling, this unit not only has high velocity, but also increased density.

435

The NE-SW oriented section (Fig. 14 – B section), is orthogonal to the well-developed sedimentary wedge of the Alpine and Apennines foredeep (PB), which is 10 km thick in the deepest part and has density values between 2350 up to 2550 kg m⁻³. Using the 2700 kg m⁻³ contour line as a marker of the top of the Mesozoic carbonate platform, it is possible to note that the contour line depth increases between latitude 46° N and latitude 44° N. The 2700 kg m⁻³ contour line reaches the surface in front of the Valsugana thrust system (at around 46° N latitude) (Fantoni and Franciosi, 2010). North of the Valsugana thrust front (VTF), corresponding to the southern alpine belt, the model shows density values of 2750 kg m⁻³ for the upper crust and 2800 up to 2900 kg m⁻³ for the middle-lower crust. In the central part of the section the model reports a very high-density plateau (RH) situated in the lower crust, that develops from the Apenninic buried thrust front (ATF) up to the outcropping south-vergent thrust (VTF).

445

The last section (close to W–E) crosses the Ivrea-Verbano area (Fig. 14 – section C), and then runs along the Po sediment basin. Lateral density variations of the upper crust are well correlated with the different basin domains represented from west to east by the Lombardian basin (LB), the Trento platform (TP) and the Belluno basin (BB). The mid-crust shows high-density (e.g. greater than 2800 kg m⁻³) values already at a depth of 20 km, and this value distribution corresponds to the previously discussed high-density ridge (RH) seen in the average density map (Fig. 14b).

450

6 Discussion

Several geophysical models have been developed for the Alpine lithosphere in the past, especially using seismic (Gebrande et al., 2006; Kästle et al., 2018) and gravity data as modeling constraints (Ebbing et al., 2006; Spooner et al., 2019). In this work for the first time, a high resolution three-dimensional seismic tomography model has been adopted as starting model for the computation of a 3D density model using the algorithm discussed before. The results show a highly complex density distribution in good agreement with the different geological domains of the Alpine area represented by the European plate, the Adriatic plate and the Tyrrhenian basin. Notwithstanding the offsets that can occur between the outcropping geology, and the intracrustal tectonic domains, we find that the average crustal density map correlates with the different tectonic realms. The Adriatic derived terrains (Southalpine and Austroalpine) of the Alps are typically denser (2850 kg m⁻³), whilst the Alpine zone composed by European terrains provenance (Helvetic and Tauern window) presents lower density values (2750 kg m⁻³). This density relation has been also noted by Spooner et al. (2019), indicating that this physical parameter could be used as a marker for the different tectonic domains.

455

460

The South-Alpine and Austroalpine provinces were the locus of sporadic, yet occasionally widespread magmatism. The magmatic occurrences are associated with strongly variable tectonic regimes, which range from clearly collision-related (the Austroalpine Paleogene plutonism, i.e., Vedrette di Ries/Riesen Ferner, Adamello, Mesino-Bragaglia), to late- or slightly post-orogenic associated with basin formations shortly after the main Variscan orogeny (Permian magmatism, e.g., the Athesian Volcanism and Ivrea Verbano and Serie dei Laghi Group), to clearly post-orogenic (Triassic, e.g., the Predazzo–Monzoni complexes), and finally to an almost within-plate environment, peripheral to the Alpine belt (the Oligocene Venetian Volcanic Province) (Bellieni et al., 2010).

These magmatic activities have undoubtedly changed the thermal setting at the time and, after cooling, increased the crustal rigidity especially in the Venetian Alps (Dolomites) which appears today the least deformed and shortened in the whole Southern Alps domain (Castellarin et al., 2006).

In this domain, south of the Dolomites, the well-known positive Bouguer gravity anomaly is present, located between the towns of Verona and Vicenza, which covers the Venetian Volcanic Province (VVP). The short-wavelength content of this gravity high can reasonably be explained by the presence of a shallow Mesozoic carbonate platform (Trento Platform) and basement which hosted several volcanic bodies, as demonstrated by field evidence and the intra-sedimentary magnetic bodies proposed by Cassano et al. (1986) on the base of magnetic and well data. According to this interpretation, the isolated mushroom-shaped body modelled in the middle-upper crust could be related to the Triassic and Cenozoic magmatic activity. These intrusions develop below the Venetian Volcanic Province and could correspond to the Predazzo–Monzoni complex and the Adamello and Mesino–Bragaglia plutons emplaced respectively in the Dolomites and westward of the South-Giudicarie fault. However, the remainder part of this signal corresponds to signal generated by the lower crustal source component, which gives origin to the long wavelength of the positive Bouguer anomaly, as also proposed by Zanolla et al. (2006). During Permian, the Austroalpine and Southalpine units were affected by magmatism, high-temperature/low-pressure metamorphism (HT-LP) and extensional tectonics. Intra-continental basins hosting Permian volcanic products have been interpreted as developed either in a late-collisional strike-slip or in a continental rifting setting (Spalla et al., 2014; Spiess et al., 2010 and references therein). Regarding the geodynamic context, all evidence suggests that this magmatic pulse was induced by post-Variscan lithospheric thinning that produced crust-mantle detachment and large ultra-mafic crustal underplating, together with the development of a Permian basin (Dal Piaz and Martin, 1998). For a fuller understanding of this process, we may refer to the modern model tested in the Western Southern Alps, in the Ivrea-Verbano zone, where the entire crustal section of an underplated and metamorphosed Hercynian basement crops out, overlain by volcanic and sediment formations (Quick et al., 2009, 1995; Sinigoi et al., 2011). In the central Southern Alps the Permian activity is represented by the porphyry plateau of the Bolzano province (Athesian plateau) and the numerous granitic–granodioritic intrusions. Considering the large scale of this process, it is reasonable to suppose the scattered presence of mafic underplating in the whole Alpine realm, confirmed by the Permian–Triassic gabbro bodies and related HT-LP metamorphism emplaced in the Austro-Alpine and South-Alpine continental crust (Spalla et al., 2014). According to this hypothesis, the high-density values modelled for the Adriatic lower crust (high-density ridge HR, Fig. 12d and 12f) are consistent with the densities of a basaltic mantle-derived rock, hence this

anomalous lower crust could be interpreted as mafic underplating emplaced between the crustal-mantle transition during Permo-Triassic post-collisional lithospheric extension.

Historically, the deep source of the Venetian positive gravity anomaly has been explained by thinned crust of 25-27 km (Cassinis, 2006; Finetti, 2005; Gebrande et al., 2006; Scarascia and Cassinis, 1997). This approach has been promoting the development of several Moho models of the Alps that invoke a relatively shallow mantle situated in the central-southern alps, especially for the gravity-modeling derived Moho models (Braitenberg et al., 2002; Ebbing et al., 2001). Recently, other seismic methodologies such as local earthquake tomography, receiver functions and ambient noise tomography, have allowed to develop 3-D high-quality crustal models of the Alps (Kästle et al., 2018; Spada et al., 2013), and this family of Moho models point to a crustal thickness of 30-35 km in the Venetian positive gravity anomaly region, corroborating the possibility that the gravimetric anomaly is related to an intra-crustal denser source (mafic underplating). Also Mueller and Talwani (1971) in their Alpine crustal model, proposed high density distribution for the South Alpine lower crust, that connects the Venetian gravity high with the Ivrea-Verbano zone.

Unfortunately, the kinematics of magmatic underplating has been described mainly by petrophysical models explaining the genesis of the outcropping rocks, while the available geophysical images of underplated material remain relatively sparse and confined to specific tectonic environments (Thybo and Artemieva, 2013). Our work adds a geophysical model based on the gravity field to demonstrate the existence of underplating to an area related to an orogen. Underplating from a gravimetric analysis had been postulated for instance also in the context of the Parana' large igneous province (Mariani et al., 2013), the Chad basin (Maddaloni et al., 2020) and the West Siberian large igneous province (Braitenberg and Ebbing, 2009).

7 Conclusion

The ~~scope~~ of this work is to study the density distribution of the Alpine lithosphere, with the specific target of characterising the sources of the well-known Venetian gravity anomaly high. A new approach based on three-dimensional seismic tomography as starting model for the computation of a 3D density model has been developed. We propose an innovative approach which includes several numerical algorithms and that provides a Moho definition, a velocity-density conversion, gravimetrical forward modeling and finally a linear inversion based on the gravimetric residual map. The results for the Alpine structure highlight that all terrains of Adriatic provenance (Austro-Alpine and South-Alpine) are denser (2850 kg m^{-3}) than the European terrains (2750 kg m^{-3}), suggesting that this physical parameter could be used as a marker to characterize the different tectonic domains involved in the Alpine regions (Spooner et al., 2019).

The studied gravity anomaly is located in the central South-Alpine domain, this area being the locus of several magmatic and volcanic activities developed from Carboniferous up to the Paleogene (Athesian Volcanic, Predazzo – Monzoni and Venetian Volcanic Province) which has modified the rheological and thermal settings. The results of our density model suggests that the gravity anomaly sources could be related to:

- Localized mushroom-shaped magmatic bodies intruded into the middle-upper crust, which could correspond to the Triassic and Cenozoic Predazzo-Monzoni, Mesino-Bregaglia and Adamello plutons, nowadays outcropping in the Southern Alps,
- Mafic underplating emplaced in the lower crust during the Permian lithosphere attenuation, similarly to the model developed for the Ivrea-Verbano complex present in the western part of the Southern Alps.

We also considered the alternative source models for this gravity anomaly, in which different authors provide a stretched and thinned Adriatic crust located between the Giudicarie thrust front and the Schio-Vicenza fault, but today several Moho models of the Alps exist, that refute this model.

The approach we use, could represent a generally applicable method to achieve insights about large-scale crustal density distributions, starting from seismic tomography, and it allowed us to carry out a high-resolution density model for the Alpine region. The expected improvement of more robust and high-resolution seismic tomography models, as well as the development of a non-linear inversion algorithm, could enhance the reliability of the density models in the future.

Appendices

TECTON Avg. SCLM comp.	
SiO ₂	44.50
TiO ₂	0.14
AlO ₃	3.50
Cr ₂ O ₃	0.40
FeO	8.0
MnO	0.13
MgO	39.8
CaO	3.10
Na ₂ O	0.24
NiO	0.26

Table A1 – Median composition of the sublithospheric continental mantle (SLCM) normalized to 100% used for the modeling of the density to seismic velocity conversion, dependent on temperature and pressure conditions (Griffin et al., 2009)

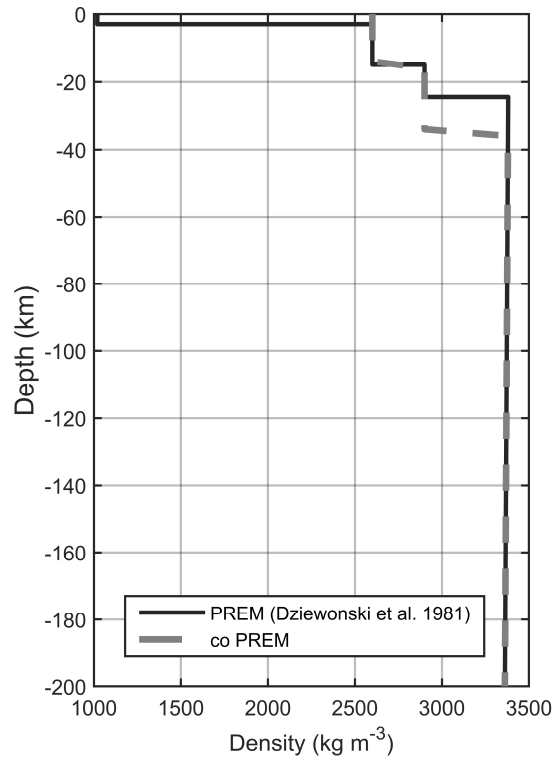


Figure A1 – Density of the PREM model and the modified coPREM model used as reference in the modeling procedure.

565

Data Availability

The 3D density model is available in the publicly accessible repository zenodo.org at link <https://www.zenodo.org/record/3885404#.Xt5IHzozbIV>.

Author Contributions

570 Both authors contributed to the conception and design of the study, manuscript writing, and approved the submitted version. Davide Tadiello was in charge of all computations.

Funding

The work was partly supported by projects ASI N. 2019-16-U.0, CUP F44117000030005 and by project PRIN 2017 20177BX42Z

575

Conflict of Interest

The authors declare that the research was conducted in the absence of any commercial or financial relationships that could be construed as a potential conflict of interest.

Acknowledgements

580 We thank E. Kästle and L. Boschi for sharing their tomographic model and for helpful discussions. We also thank for helpful discussions on the petrologic modeling M. Velicogna, A. De Min, M. Tesauero and for assistance in using the Perple_X software L. Ziberna. T. Pivetta and A. Pastorutti are thanked for assistance in Matlab programming and helpful discussions. We thank two anonymous reviewers for dedicating their time for two thoughtful reviews, published alongside our work.

References

- 585 Abbas, H., Michail, M., Cifelli, F., Mattei, M., Gianolla, P., Lustrino, M., Carminati, E., 2018. Emplacement modes of the Ladinian plutonic rocks of the Dolomites: Insights from anisotropy of magnetic susceptibility. *Journal of Structural Geology* 113, 42–61. <https://doi.org/10.1016/j.jsg.2018.05.012>
- AlpArray Seismic Network, 2015. AlpArray Seismic Network (AASN) temporary component. https://doi.org/10.12686/ALPARRAY/Z3_2015
- 590 Andersen, O.B., 2010. The DTU10 Gravity field and Mean sea surface. Presented at the Second international symposium of the gravity field of the Earth (IGFS2), Fairbanks, Alaska., Second international symposium of the gravity field of the Earth (IGFS2), Fairbanks, Alaska.
- Andersen, O.B., Knudsen, P., Berry, P.A.M., 2010. The DNSC08GRA global marine gravity field from double retracked satellite altimetry. *J Geod* 84, 191–199. <https://doi.org/10.1007/s00190-009-0355-9>
- 595 Anderson, E.G., 1976. Anderson EG (1976) The effect of topography on solutions of Stokes' problem. Unisurv S-14, Rep, School of Surveying, University of New South Wales, Australia.
- Bai, Z., Zhang, S., Braitenberg, C., 2013. Crustal density structure from 3D gravity modeling beneath Himalaya and Lhasa blocks, Tibet. *Journal of Asian Earth Sciences* 78, 301–317. <https://doi.org/10.1016/j.jseaes.2012.12.035>
- Barthelmes, F., 2013. Definition of Functionals of the Geopotential and Their Calculation from Spherical Harmonic Models. Scientific Technical Report (STR) STR 09/02, 1–32. <https://doi.org/10.2312/GFZ.b103-0902-26>
- 600 Bellieni, G., Fioretti, A.M., Marzoli, A., Visonà, D., 2010. Permo–Paleogene magmatism in the eastern Alps. *Rend. Fis. Acc. Lincei* 21, 51–71. <https://doi.org/10.1007/s12210-010-0095-z>
- Bertotti, G., Picotti, V., Bernoulli, D., Castellarin, A., 1993. From rifting to drifting: tectonic evolution of the South-Alpine upper crust from the Triassic to the Early Cretaceous. *Sedimentary Geology* 86, 53–76. [https://doi.org/10.1016/0037-0738\(93\)90133-P](https://doi.org/10.1016/0037-0738(93)90133-P)
- 605 Bigi, G., Castellarin, A., Coli, M., Dal Piaz, G.V., Sartori, R., Scandone, P., Vai, G.B., 1990a. Structural Model of Italy scale 1:500.000, sheet 1. Structural Model of Italy scale 1:500.000, sheet 1.
- Bigi, G., Castellarin, A., Coli, M., Dal Piaz, G.V., Vai, G.B., 1990b. Structural Model of Italy scale 1:500.000, sheet 2. Structural Model of Italy scale 1:500.000, sheet 2.
- 610 Braitenberg, C., Ebbing, J., 2009. New insights into the basement structure of the West Siberian Basin from forward and inverse modeling of GRACE satellite gravity data. *Journal of Geophysical Research: Solid Earth* 114. <https://doi.org/10.1029/2008JB005799>
- Braitenberg, C., Ebbing, J., Götze, H.-J., 2002. Inverse modelling of elastic thickness by convolution method - The eastern Alps as a case example. *Earth and Planetary Science Letters* 202, 387–404. [https://doi.org/10.1016/S0012-821X\(02\)00793-8](https://doi.org/10.1016/S0012-821X(02)00793-8)
- 615 Braitenberg, C., Mariani, P., De Min, A., 2013. The European Alps and Nearby Orogenic Belts Sensed by GOCE. *Boll. Geofis. Teor. Appl.* 54, 321–334. <https://doi.org/10.4430/bgta0105>

- Brocher, T.M., 2005. Empirical Relations between Elastic Wavespeeds and Density in the Earth's Crust. *Bulletin of the Seismological Society of America* 95, 2081–2092. <https://doi.org/10.1785/0120050077>
- 620 Casetta, F., Coltorti, M., Marrocchino, E., 2018. Petrological evolution of the Middle Triassic Predazzo Intrusive Complex, Italian Alps. *International Geology Review* 60, 977–997. <https://doi.org/10.1080/00206814.2017.1363676>
- Cassano, E., Anelli, L., Fichera, R., Cappelli, V., 1986. Pianura Padana: interpretazione integrata di dati geofisici e geologici. Presented at the 73° Congresso Società Geologica Italiana, Roma, 29 Settembre - 4 ottobre 1986, pp. 1–28.
- Cassinis, R., 2006. Reviewing pre-TRANSALP DSS models. *Tectonophysics*, TRANSALP 414, 79–86. <https://doi.org/10.1016/j.tecto.2005.10.026>
- 625 Castellarin, A., Cantelli, L., 2000. Neo-Alpine evolution of the Southern Eastern Alps. *Journal of Geodynamics* 30, 251–274. [https://doi.org/10.1016/S0264-3707\(99\)00036-8](https://doi.org/10.1016/S0264-3707(99)00036-8)
- Castellarin, A., Vai, G.B., Cantelli, L., 2006. The Alpine evolution of the Southern Alps around the Giudicarie faults: A Late Cretaceous to Early Eocene transfer zone. *Tectonophysics* 414, 203–223. <https://doi.org/10.1016/j.tecto.2005.10.019>
- 630 Christensen, N.I., Mooney, W.D., 1995. Seismic velocity structure and composition of the continental crust: A global view. *Journal of Geophysical Research: Solid Earth* 100, 9761–9788. <https://doi.org/10.1029/95JB00259>
- Connolly, J.A.D., 2005. Computation of phase equilibria by linear programming: A tool for geodynamic modeling and its application to subduction zone decarbonation. *Earth and Planetary Science Letters* 236, 524–541. <https://doi.org/10.1016/j.epsl.2005.04.033>
- 635 Dal Piaz, G.V., Bistacchi, A., Massironi, M., 2003. Geological outline of the Alps. *Episodes* 26, 175–180. <https://doi.org/10.18814/epiugs/2003/v26i3/004>
- Dal Piaz, G.V., Martin, S., 1998. Evoluzione litosferica e magmatismo nel dominio austro-sudalpino dall'orogenesi varisica al rifting mesozoico. *Memorie della Società Geologica Italiana* 53, 43–62.
- De Min, A., Velicogna, M., Ziberna, L., Chiaradia, M., Alberti, A., Marzoli, A., 2020. Triassic magmatism in the European Southern Alps as an early phase of Pangea break-up. *Geol. Mag.* 1–23. <https://doi.org/10.1017/S0016756820000084>
- 640 Ebbing, J., Braitenberg, C., Götze, H.-J., 2006. The lithospheric density structure of the Eastern Alps. *Tectonophysics* 414, 145–155. <https://doi.org/10.1016/j.tecto.2005.10.015>
- Ebbing, J., Braitenberg, C., Götze, H.-J., 2001. Forward and inverse modelling of gravity revealing insight into crustal structures of the Eastern Alps. *Tectonophysics* 337, 191–208. [https://doi.org/10.1016/S0040-1951\(01\)00119-6](https://doi.org/10.1016/S0040-1951(01)00119-6)
- 645 Ekström, G., 2011. A global model of Love and Rayleigh surface wave dispersion and anisotropy, 25–250 s: Global dispersion model GDM52. *Geophysical Journal International* 187, 1668–1686. <https://doi.org/10.1111/j.1365-246X.2011.05225.x>
- Fantoni, R., Franciosi, R., 2010. Tectono-sedimentary setting of the Po Plain and Adriatic foreland. *Rend. Fis. Acc. Lincei* 21, 197–209. <https://doi.org/10.1007/s12210-010-0102-4>
- 650 Finetti, I.R., 2005. Depth Contour Map of the Moho Discontinuity in the Central Mediterranean Region from New CROP Seismic Data. Presented at the Finetti, I.R. (Ed.) CROP Project: Deep Seismic Exploration of the Central Mediterranean and Italy, Elsevier, *Atlases in Geoscience*, Amsterdam, Netherlands, pp. 597–606.
- Förste, C., Bruinsma, S., Abrikosov, O., Flechtner, F., Marty, J.-C., Lemoine, J.-M., Dahle, C., Neumayer, H., Barthelmes, F., König, R., others, 2014a. EIGEN-6C4-The latest combined global gravity field model including GOCE data up to degree and order 1949 of GFZ Potsdam and GRGS Toulouse, in: EGU General Assembly Conference Abstracts.
- 655 Förste, C., Bruinsma, Sean.L., Abrikosov, O., Lemoine, J.-M., Marty, J.C., Flechtner, F., Balmino, G., Barthelmes, F., Biancale, R., 2014b. EIGEN-6C4 The latest combined global gravity field model including GOCE data up to degree and order 2190 of GFZ Potsdam and GRGS Toulouse. <https://doi.org/10.5880/icgem.2015.1>
- Gardner, G.H.F., Gardner, L.W., Gregory, A.R., 1974. FORMATION VELOCITY AND DENSITY—THE DIAGNOSTIC BASICS FOR STRATIGRAPHIC TRAPS. *GEOPHYSICS* 39, 770–780. <https://doi.org/10.1190/1.1440465>
- 660 Gebrande, H., Castellarin, A., Lüschen, E., Millahn, K., Neubauer, F., Nicolich, R., 2006. TRANSALP—A transect through a young collisional orogen: Introduction. *Tectonophysics*, TRANSALP 414, 1–7. <https://doi.org/10.1016/j.tecto.2005.10.030>
- Grad, M., Tiira, T., ESC Working Group, 2009. The Moho depth map of the European Plate. *Geophysical Journal International* 176, 279–292. <https://doi.org/10.1111/j.1365-246X.2008.03919.x>
- 665 Griffin, W.L., O'Reilly, S.Y., Afonso, J.C., Begg, G.C., 2009. The Composition and Evolution of Lithospheric Mantle: a Re-evaluation and its Tectonic Implications. *J Petrology* 50, 1185–1204. <https://doi.org/10.1093/petrology/egn033>

- Grombein, T., Seitz, K., Heck, B., 2013. Optimized formulas for the gravitational field of a tesseroid. *Journal of Geodesy* 87, 645–660. <https://doi.org/10.1007/s00190-013-0636-1>
- 670 Heck, B., Seitz, K., 2007. A comparison of the tesseroid, prism and point-mass approaches for mass reductions in gravity field modelling. *J Geod* 81, 121–136. <https://doi.org/10.1007/s00190-006-0094-0>
- Hirt, C., Rexer, M., 2015. Earth2014: 1 arc-min shape, topography, bedrock and ice-sheet models – Available as gridded data and degree-10,800 spherical harmonics. *International Journal of Applied Earth Observation and Geoinformation* 39, 103–112. <https://doi.org/10.1016/j.jag.2015.03.001>
- 675 Holland, T.J.B., Powell, R., 1998. An internally consistent thermodynamic data set for phases of petrological interest. *Journal of Metamorphic Geology* 16, 309–343. <https://doi.org/10.1111/j.1525-1314.1998.00140.x>
- Kästle, E.D., El-Sharkawy, A., Boschi, L., Meier, T., Rosenberg, C., Bellahsen, N., Cristiano, L., Weidle, C., 2018. Surface Wave Tomography of the Alps Using Ambient-Noise and Earthquake Phase Velocity Measurements. *Journal of Geophysical Research: Solid Earth* 123, 1770–1792. <https://doi.org/10.1002/2017JB014698>
- 680 Kennett, B.L.N., Engdahl, E.R., Buland, R., 1995. Constraints on seismic velocities in the Earth from traveltimes. *Geophysical Journal International* 122, 108–124. <https://doi.org/10.1111/j.1365-246X.1995.tb03540.x>
- Laske, G., Masters, G., Ma, Z., Pasyanos, M., 2013. Update on CRUST1.0 - A 1-degree Global Model of Earth's Crust. Presented at the EGU General Assembly 2013, 7-12 April, 2013, Vienna, Austria, *Geophys Res Abstracts*, pp. EGU2013-2658.
- 685 Macera, P., Gasperini, D., Ranalli, G., Mahatsente, R., 2008. Slab detachment and mantle plume upwelling in subduction zones: An example from the Italian South-Eastern Alps. *Journal of Geodynamics* 45, 32–48. <https://doi.org/10.1016/j.jog.2007.03.004>
- Maddaloni, F., Pivetta, T., Braitenberg, C., 2020. Gravimetry and petrophysics for defining the intracratonic and rift basins of the western-central Africa zone., *Geophysics*, under Review, GEO-2019-0522.R1.
- 690 Mariani, P., Braitenberg, C., Ussami, N., 2013. Explaining the thick crust in Paraná basin, Brazil, with satellite GOCE gravity observations. *Journal of South American Earth Sciences* 45, 209–223. <https://doi.org/10.1016/j.jsames.2013.03.008>
- Martin, S., Macera, P., 2014. Tertiary volcanism in the Italian Alps (Giudicarie fault zone, NE Italy): insight for double alpine magmatic arc. *Italian Journal of Geosciences* 133, 63–84. <https://doi.org/10.3301/IJG.2013.14>
- Milani, L., Beccaluva, L., Coltorti, M., 1999. Petrogenesis and evolution of the Euganean Magmatic Complex, Veneto Region, North-East Italy. *European Journal of Mineralogy* 11, 379–400. <https://doi.org/10.1127/ejm/11/2/0379>
- 695 Mooney, W.D., 2007. 1.11 Crust and Lithospheric Structure – Global Crustal Structure, in: *Treatise on Geophysics*, Volume 1. Seismology and the Structure of the Earth. Schubert G., p. 57.
- Mueller, S., Talwani, M., 1971. A crustal section across the Eastern Alps based on gravity and seismic refraction data. *PAGEOPH* 85, 226–239. <https://doi.org/10.1007/BF00875411>
- 700 Muttoni, G., Gaetani, M., Kent, D.V., Sciunnach, D., Berra, F., Garzanti, E., Mattei, M., Zanchi, A., 2009. Opening of the Neo-Tethys Ocean and the Pangea B to Pangea A transformation during the Permian. *GeoArabia* 14, 17–48.
- Pavlis, N.K., Holmes, S.A., Kenyon, S.C., Factor, J.K., 2012. The development and evaluation of the Earth Gravitational Model 2008 (EGM2008). *Journal of Geophysical Research: Solid Earth* 117. <https://doi.org/10.1029/2011JB008916>
- Pfiffner, A., 2015. *Geologie der Alpen*, Dritte Aufl. ed. Haupt Verlag.
- 705 Quick, J.E., Sinigoi, S., Mayer, A., 1995. Emplacement of mantle peridotite in the lower continental crust, Ivrea-Verbano zone, northwest Italy. *Geology* 23, 739–742. [https://doi.org/10.1130/0091-7613\(1995\)023<0739:EOMPIT>2.3.CO;2](https://doi.org/10.1130/0091-7613(1995)023<0739:EOMPIT>2.3.CO;2)
- Quick, J.E., Sinigoi, S., Peressini, G., Demarchi, G., Wooden, J.L., Sbisà, A., 2009. Magmatic plumbing of a large Permian caldera exposed to a depth of 25 km. *Geology* 37, 603–606. <https://doi.org/10.1130/G30003A.1>
- Rexer, M., Hirt, C., Claessens, S., Tenzer, R., 2016. Layer-Based Modelling of the Earth's Gravitational Potential up to 10-km Scale in Spherical Harmonics in Spherical and Ellipsoidal Approximation. *Surv Geophys* 37, 1035–1074. <https://doi.org/10.1007/s10712-016-9382-2>
- 710 Rosenberg, C.L., Kissling, E., 2013. Three-dimensional insight into Central-Alpine collision: Lower-plate or upper-plate indentation? *Geology* 41, 1219–1222. <https://doi.org/10.1130/G34584.1>
- Rottura, A., Bargossi, G.M., Caggianelli, A., Del Moro, A., Visonà, D., Tranne, C.A., 1998. Origin and significance of the Permian high-K calc-alkaline magmatism in the central-eastern Southern Alps, Italy. *Lithos* 45, 329–348. [https://doi.org/10.1016/S0024-4937\(98\)00038-3](https://doi.org/10.1016/S0024-4937(98)00038-3)
- 715

- Scarascia, S., Cassinis, R., 1997. Crustal structures in the central-eastern Alpine sector: A revision of the available DSS data. *Tectonophysics* 271, 157–188. [https://doi.org/10.1016/S0040-1951\(96\)00206-5](https://doi.org/10.1016/S0040-1951(96)00206-5)
- 720 Schuster, R., Stüwe, K., 2008. Permian metamorphic event in the Alps. *Geology* 36, 603–606. <https://doi.org/10.1130/G24703A.1>
- Sinigoi, S., Quick, J.E., Demarchi, G., Klötzli, U., 2011. The role of crustal fertility in the generation of large silicic magmatic systems triggered by intrusion of mantle magma in the deep crust. *Contrib Mineral Petrol* 162, 691–707. <https://doi.org/10.1007/s00410-011-0619-2>
- 725 Spada, M., Bianchi, I., Kissling, E., Agostinetti, N.P., Wiemer, S., 2013. Combining controlled-source seismology and receiver function information to derive 3-D moho topography for Italy. *Geophysical Journal International* 194, 1050–1068. <https://doi.org/10.1093/gji/ggt148>
- Spalla, M.I., Zanon, D., Marotta, A.M., Rebay, G., Roda, M., Zucali, M., Gosso, G., 2014. The transition from Variscan collision to continental break-up in the Alps: insights from the comparison between natural data and numerical model predictions. *Geological Society, London, Special Publications* 405, 363. <https://doi.org/10.1144/SP405.11>
- 730 Spiess, R., Cesare, B., Mazzoli, C., Sassi, R., Sassi, F.P., 2010. The crystalline basement of the Adria microplate in the eastern Alps: a review of the palaeostructural evolution from the Neoproterozoic to the Cenozoic. *RENDICONTI LINCEI* 21, 31–50. <https://doi.org/10.1007/s12210-010-0100-6>
- Spooner, C., Scheck-Wenderoth, M., Götze, H.-J., Ebbing, J., Hetényi, G., 2019. Density distribution across the Alpine lithosphere constrained by 3D gravity modelling and relation to seismicity and deformation. *Solid Earth Discuss.* 1–26. <https://doi.org/10.5194/se-2019-115>
- 735 Stampfli, G.M., Borel, G.D., 2002. A plate tectonic model for the Paleozoic and Mesozoic constrained by dynamic plate boundaries and restored synthetic oceanic isochrons. *Earth and Planetary Science Letters* 196, 17–33. [https://doi.org/10.1016/S0012-821X\(01\)00588-X](https://doi.org/10.1016/S0012-821X(01)00588-X)
- Steinberger, B., Werner, S.C., Torsvik, T.H., 2010. Deep versus shallow origin of gravity anomalies, topography and volcanism on Earth, Venus and Mars. *Icarus* 207, 564–577. <https://doi.org/10.1016/j.icarus.2009.12.025>
- 740 Szwillus, W., Ebbing, J., Holzrichter, N., 2016. Importance of far-field topographic and isostatic corrections for regional density modelling. *Geophys J Int* 207, 274–287. <https://doi.org/10.1093/gji/ggw270>
- Tenzer, R., Foughi, I., Hirt, C., Novák, P., Pitoňák, M., 2019. How to Calculate Bouguer Gravity Data in Planetary Studies. *Surveys in Geophysics* 40, 107–132. <https://doi.org/10.1007/s10712-018-9504-0>
- 745 Tesauero, M., Kaban, M.K., Cloetingh, S.A.P.L., 2008. EuCRUST-07: A new reference model for the European crust. *Geophysical Research Letters* 35. <https://doi.org/10.1029/2007GL032244>
- Torge, W., 2011. *Geodesy*, 3rd compl. rev. and extend. ed. ed. De Gruyter, Berlin, Boston. <https://doi.org/10.1515/9783110879957>
- Torge, W., Müller, J., 2012. *Geodesy*, 4th ed. ed. De Gruyter, Berlin, Boston. <https://doi.org/10.1515/9783110250008>
- 750 Uieda, L., Barbosa, V.C.F., Braitenberg, C., 2016. Tesseroids: Forward-modeling gravitational fields in spherical coordinates. *GEOPHYSICS* 81, F41–F48. <https://doi.org/10.1190/geo2015-0204.1>
- Vaniček, P., Tenzer, R., Sjöberg, L.E., Martinec, Z., Featherstone, W.E., 2004. New views of the spherical Bouguer gravity anomaly. *Geophysical Journal International* 159, 460–472. <https://doi.org/10.1111/j.1365-246X.2004.02435.x>
- 755 Viganò, A., Scafidi, D., Martin, S., Spallarossa, D., 2013. Structure and properties of the Adriatic crust in the central-eastern Southern Alps (Italy) from local earthquake tomography. *Terra Nova* 25, 504–512. <https://doi.org/10.1111/ter.12067>
- Wild-Pfeiffer, F., 2008. A comparison of different mass elements for use in gravity gradiometry. *J Geod* 82, 637–653. <https://doi.org/10.1007/s00190-008-0219-8>
- Zampieri, D., 1995. Tertiary extension in the southern Trento Platform, Southern Alps, Italy. *Tectonics* 14, 645–657. <https://doi.org/10.1029/94TC03093>
- 760 Zanchetta, S., Garzanti, E., Doglioni, C., Zanchi, A., 2012. The Alps in the Cretaceous: a doubly vergent pre-collisional orogen: The Alps in the Cretaceous. *Terra Nova* 24, 351–356. <https://doi.org/10.1111/j.1365-3121.2012.01071.x>
- Zanolla, C., Braitenberg, C., Ebbing, J., Bernabini, M., Bram, K., Gabriel, G., Götze, H.-J., Giammetti, S., Meurers, B., Nicolich, R., Palmieri, F., 2006. New gravity maps of the Eastern Alps and significance for the crustal structures. *Tectonophysics* 414, 127–143. <https://doi.org/10.1016/j.tecto.2005.10.012>

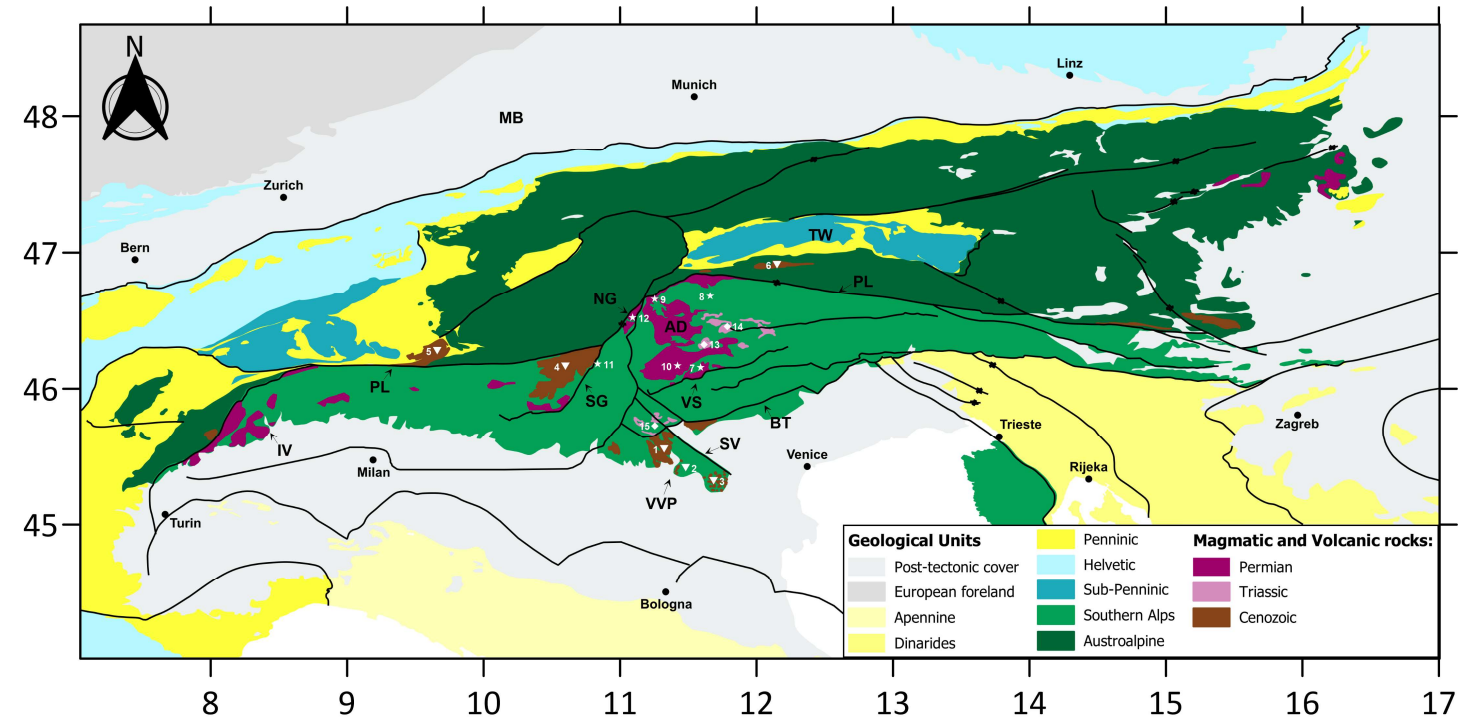


Figure 1 – Geologic chart of the Alps modified after (Pfiffner, 2015) and main magmatic and volcanic bodies (Bigi et al., 1990a, 1990b; Schuster and Stüwe, 2008). VVP: Venetian Volcanic Province; SV: Schio-Vicenza Fault; BT: Bassano-Montello Thrusts; VS: Val Sugana Thrust; SG: South Giudicarie Fault; NG: North Giudicarie Fault; AD: Athesian Volcanic District; PL: Periadriatic Line; IV: Ivrea-Verbano Complex; TW: Tauern Window; MB: Molasse Basin. 1) Lessini Mountains; 2) Berici Hills; 3) Euganei Hills; 4) Adamello Batholith; 5) Mesino-Bragaglia Batholith; 6) Vedrette di Ries/Riesen Ferner Batholith; 7) Cima d'Asta Intrusion; 8) Bressanone-Chiusa Intrusions; 9) Ivigna Intrusion; 10) Monte Croce Intrusion; 11) Monte Sabion Intrusion; 12) Monte Luco Intrusion; 13) Predazzo Intrusion; 14) Monzoni Intrusion; 15) Recoaro-Pasubio Intrusions.

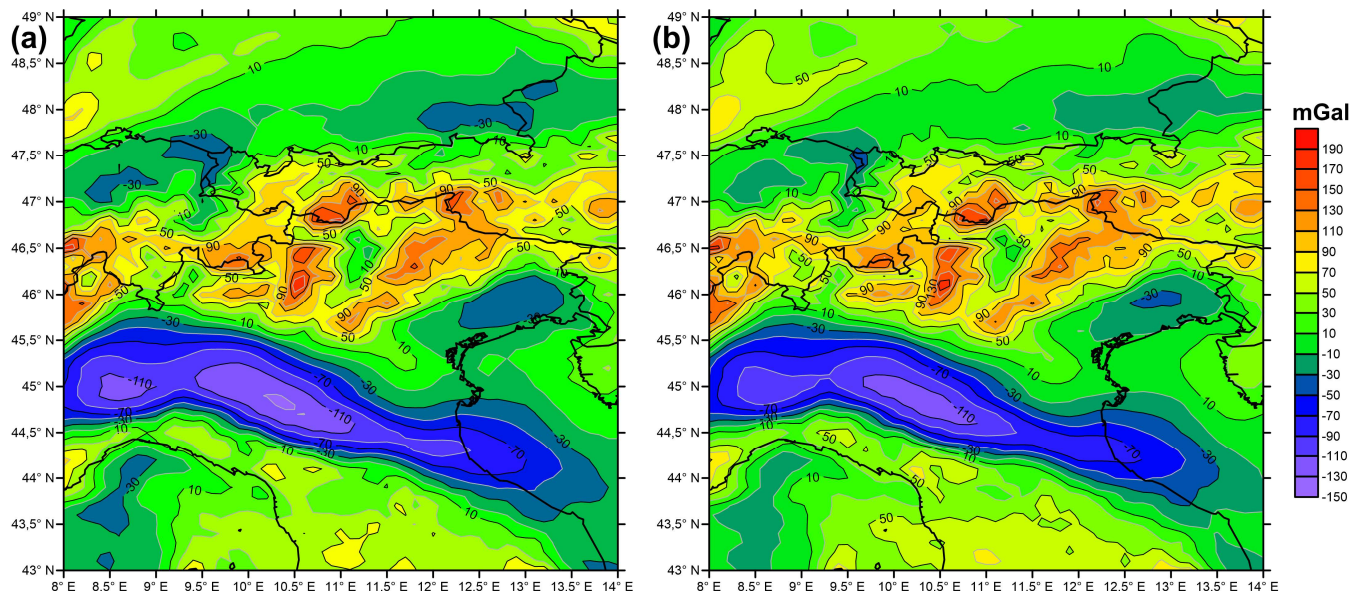


Figure 2 – a) Gravity anomaly; b) Gravity disturbance; both functionals have been calculated with the gravity model EIGEN6c4 (Förste et al., 2014a); maximum degree $N = 2190$ and calculation height $h = 5000$ m.

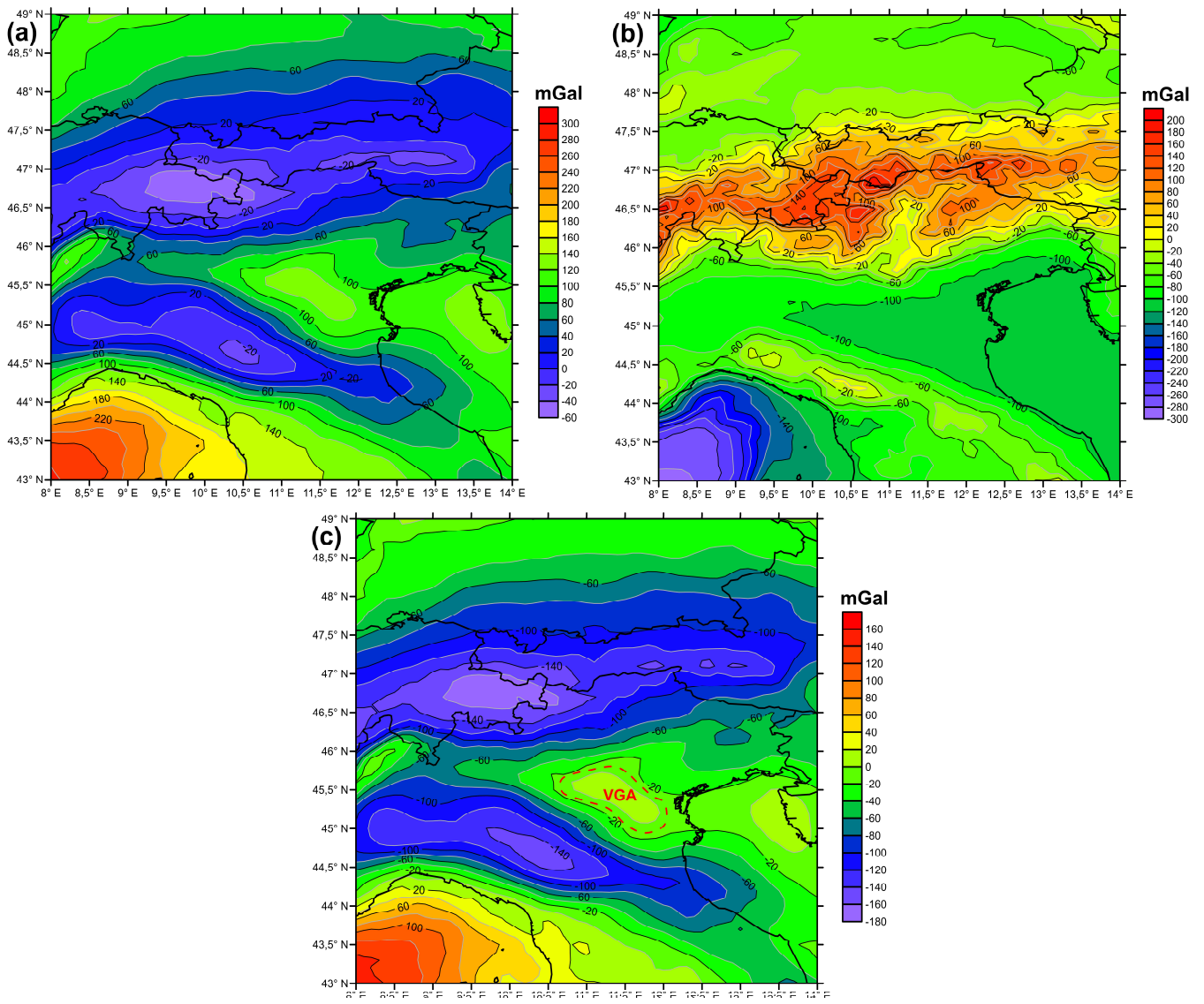


Figure 3 – a) Bouguer gravity disturbance, using gravity model EIGEN6c4 corrected with topography model RET2014 (N = 2190 and calculation height h = 5000m), b) Gravity disturbance of the model RET2014 (Rexer et al., 2016) (with N = 2190 and calculation height h = 5000m), c) Band-limited Bouguer gravity disturbance, using gravity model EIGEN6c4 corrected with topography model RET2014 (both calculated with $10 < N \leq 2190$ and calculation height h = 5000m). VGA: Venetian Positive Gravity Anomaly.

	V_{Smin}	V_{Smax}	V_{Smean}	σ (std)	$V_{Smin} - \sigma$	$V_{Smax} - \sigma$
Crust1.0	3.650	4.685	4.069	0.173	3.896	4.242
EuCrust07	3.539	4.718	4.070	0.233	3.837	4.303
MohoGrad	3.524	4.725	4.110	0.209	3.901	4.318

Table 1 – Statistics of the S-wave velocity (km s^{-1}) of tomographic model (Kästle et al., 2018), at the depths of Moho defined in three Moho models (Grad et al., 2009) (MohoGrad), (Tesauro et al., 2008) (EuCrust07) and (Laske et al., 2013)(Crust1.0). Average value (V_{Smean}), Minimum value (V_{Smin}), Maximum value (V_{Smax}), σ (standard deviation) in km s^{-1} .

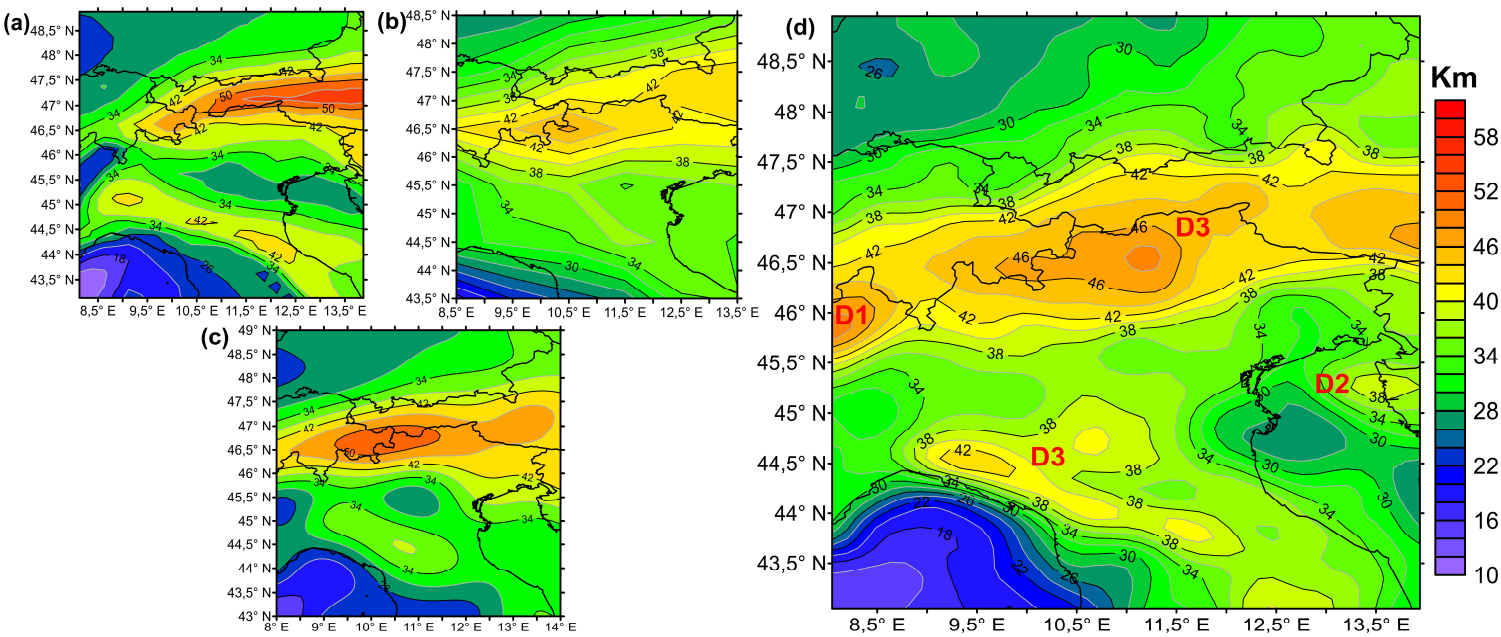


Figure 4 - Map of the Moho depth according to: a) EuCrust07 (Tesauro et al., 2008), b) CRUST1.0 (Laske et al., 2013), c) MohoGrad (Grad et al., 2009) and d) MohoTad (this work).

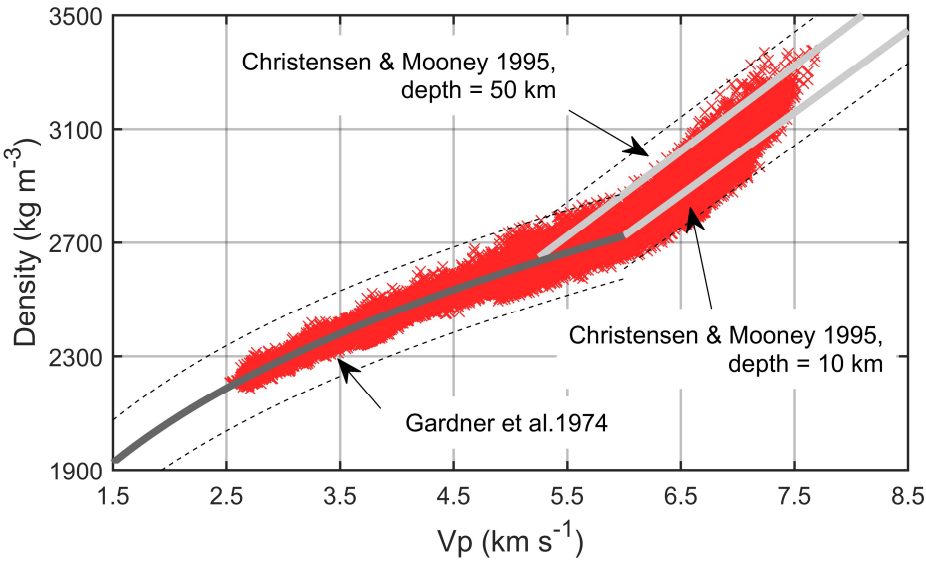


Figure 5 –Comparison of published densities versus V_p relations discussed in (Brocher, 2005), dark grey continuous line represents the Gardner's equation, light grey continuous line represents Christensen & Mooney (1995) linear regression fit. The relation of Christensen and Mooney (1995) has been published for different depth ranges, from 10 to 50 km, and we show the two extreme relations. The stippled curves delimit the upper and lower bounds derived from the root mean square experimental scatter from the lines. The switch from Gardner's equation to the relation of Christensen and Mooney is made at the intersection of the two relations. The red symbols show the final distribution of the density versus velocity values of our final model, at the end of the iterations.

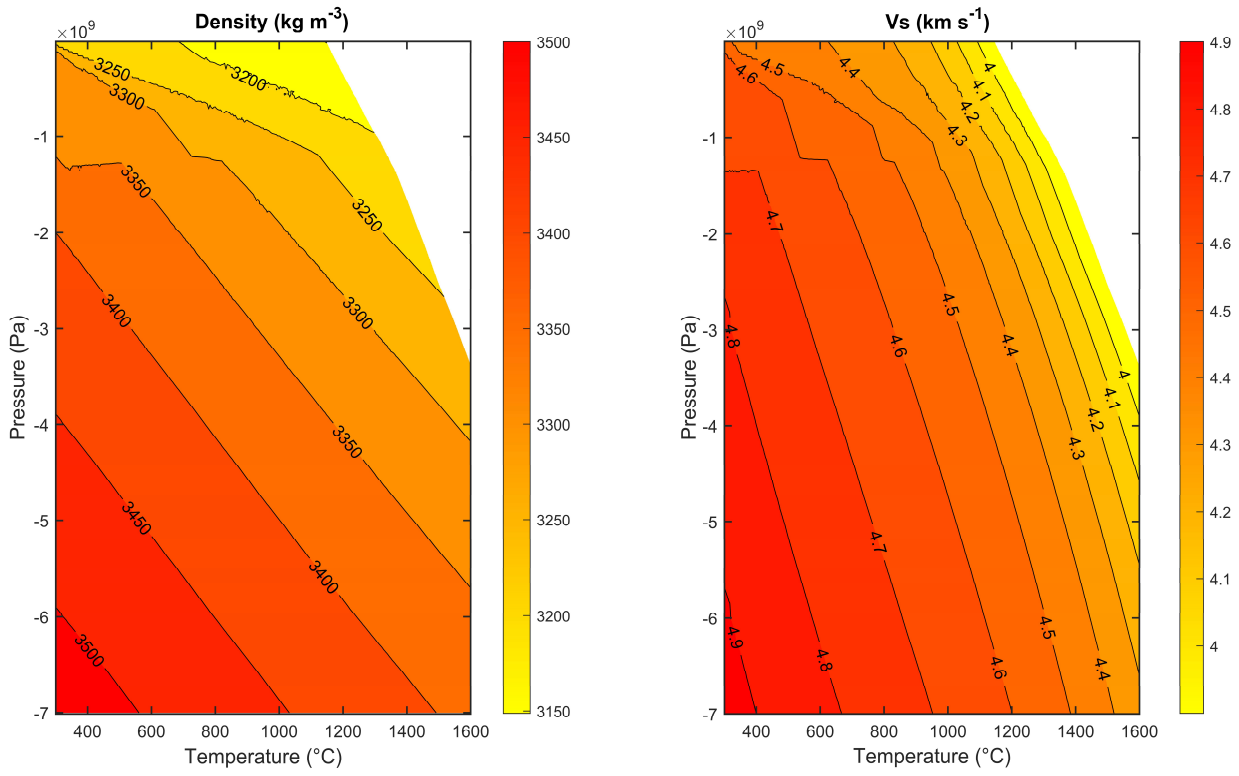


Figure 6 – Density and Vs plots of the model SUM as functions of pressure and temperature.

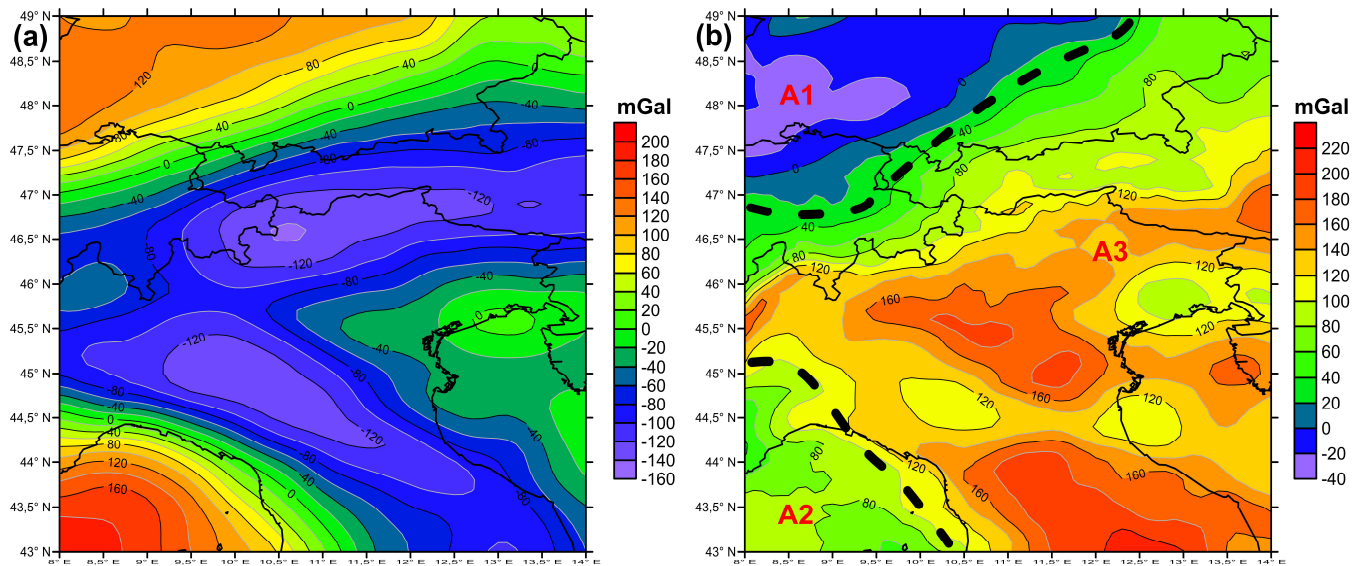


Figure 7 – a) Gravity anomaly map from the forward modeling, b) residual gravity map obtained from the difference between the Bouguer gravity disturbance (with $10 < N \leq 2190$) and the forward gravity anomaly map. A1: Germany and Switzerland negative residual region; A2: positive residual region of Tyrrhenian basin; A3: Adriatic and Alpine domain characterized by high residual, black dashed lines divide the three different regions.

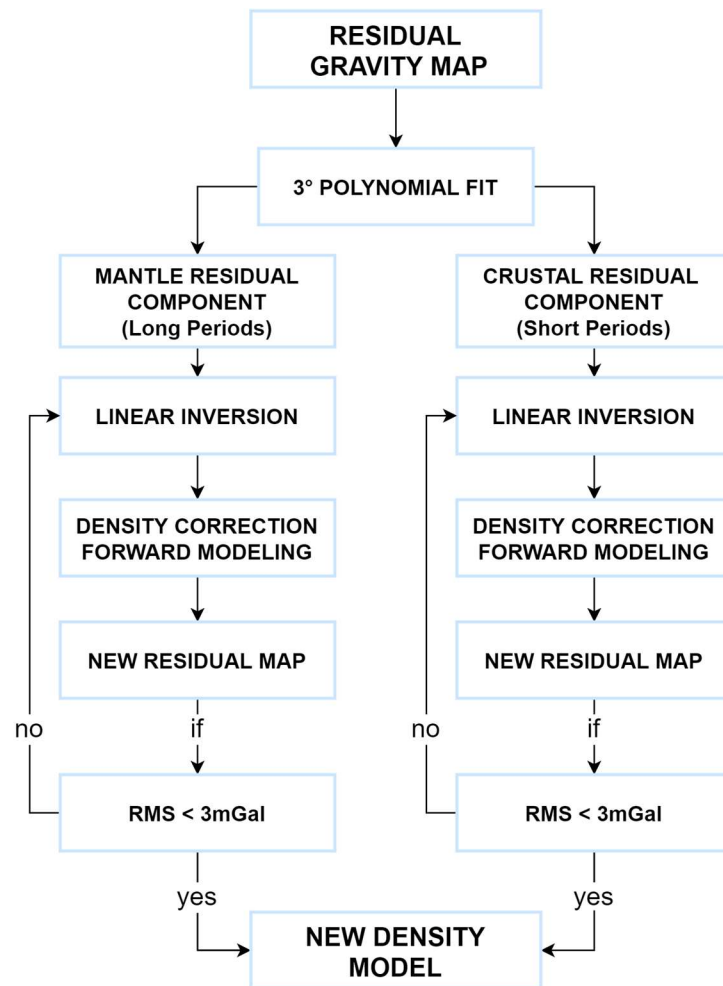


Figure 8 – Flowchart of the linear inversion algorithm

840

845

850

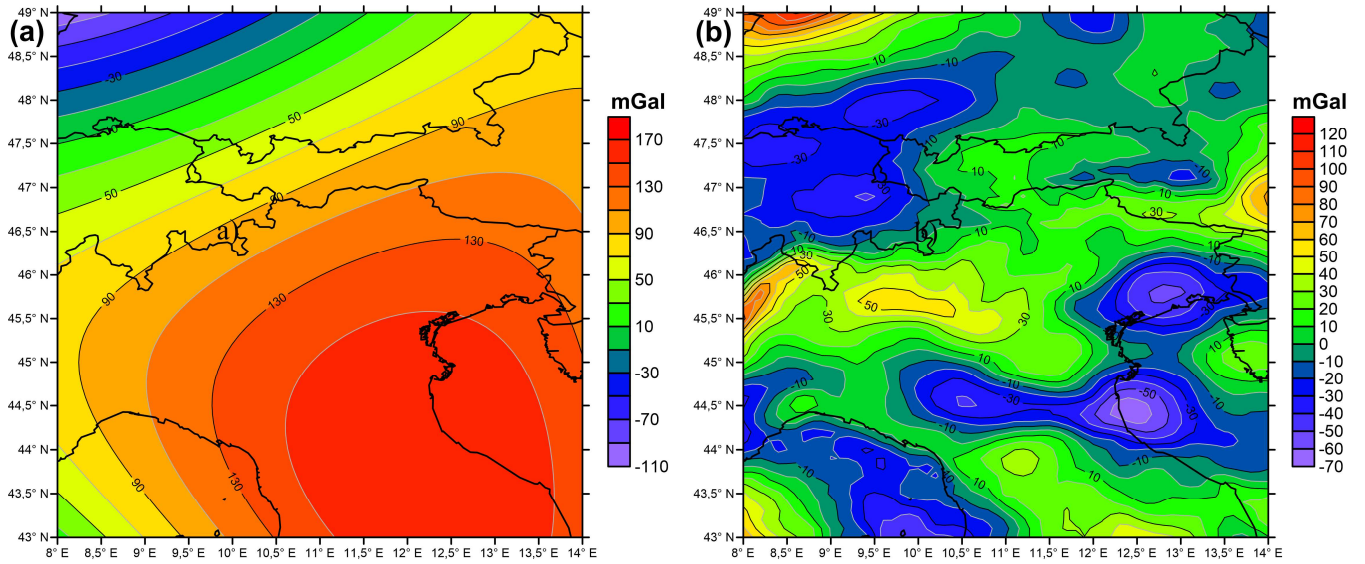


Figure 9 – a) Mantle residual component map (long-periods), b) Crustal residual component maps (short-periods)

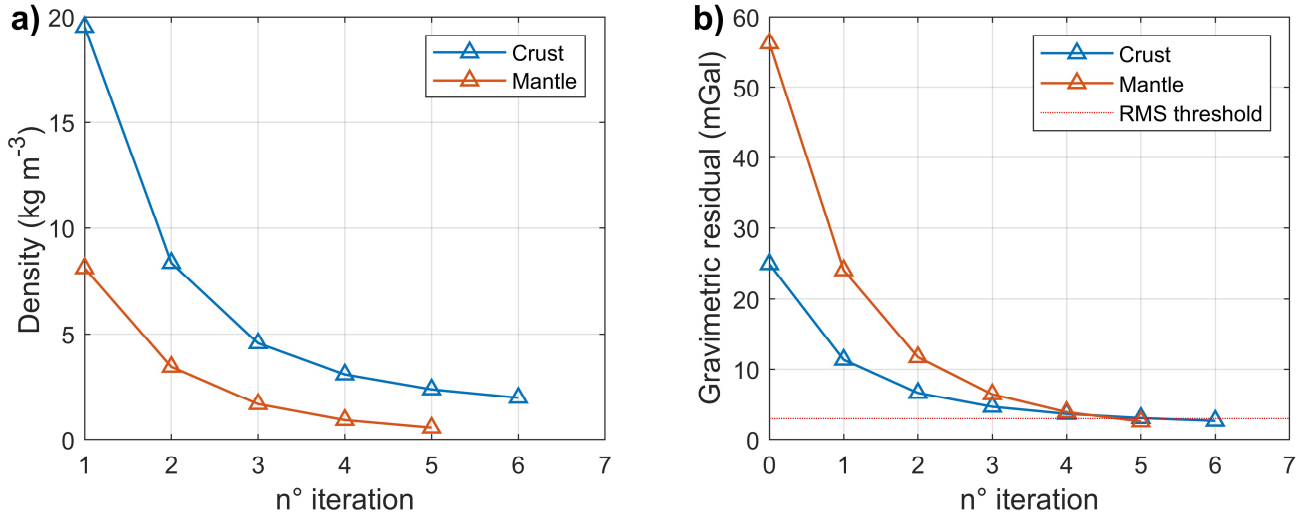


Figure 10 – Illustration of the effectiveness of the iteration steps in crust and mantle. a) Root means square density correction over the volume of crust and mantle during iterations. b) Root mean square decrease of the gravity residual, separated for the signal of crust and mantle during iterations. The iterations were stopped when a root mean square residual of 3 mGal was reached.

855

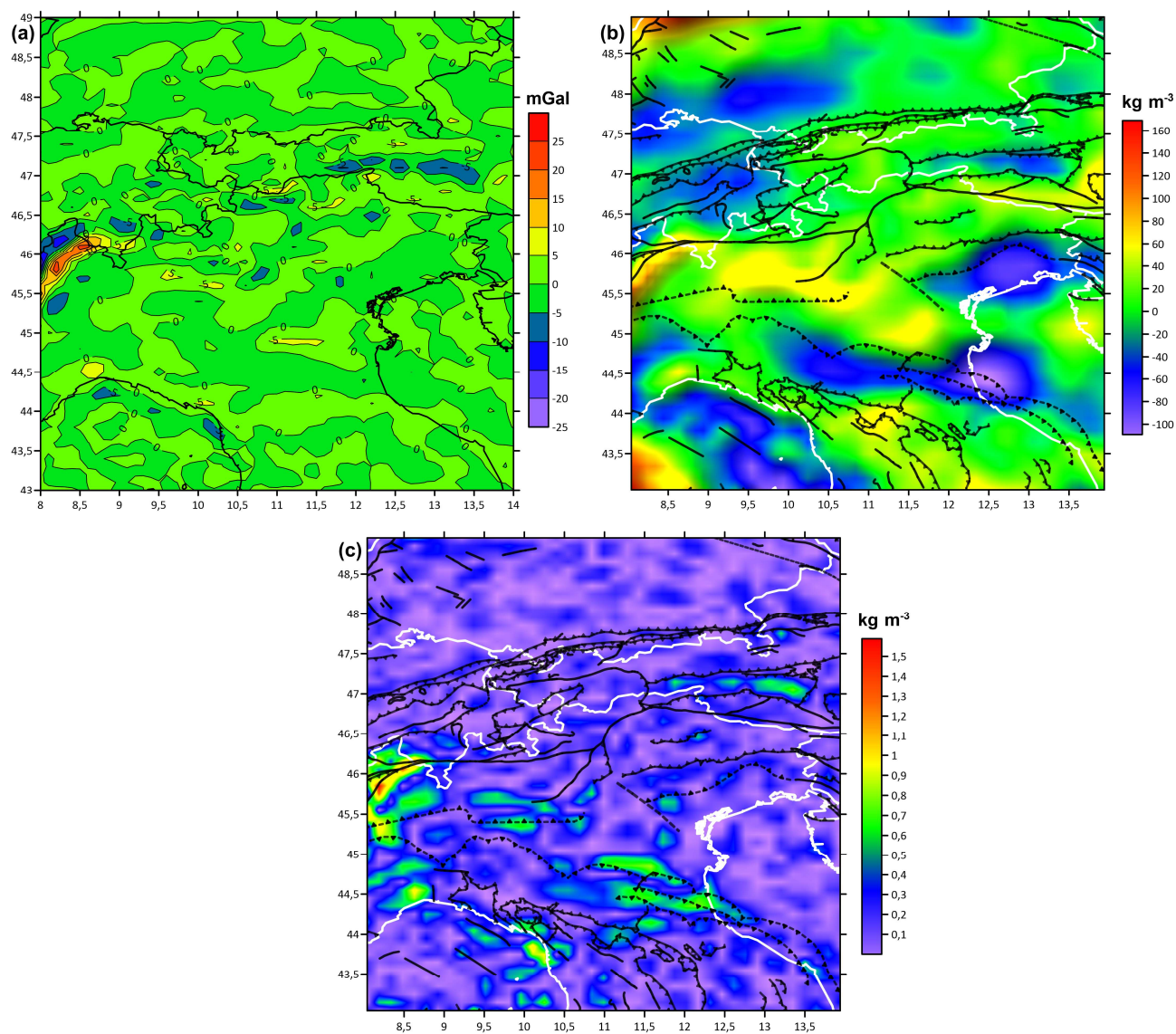


Figure 11 – a) Final gravity residual after crustal inversion, b) Sum of density corrections obtained during crustal inversion, c) Root mean square value of the density uncertainty along the crustal column after the final correction.

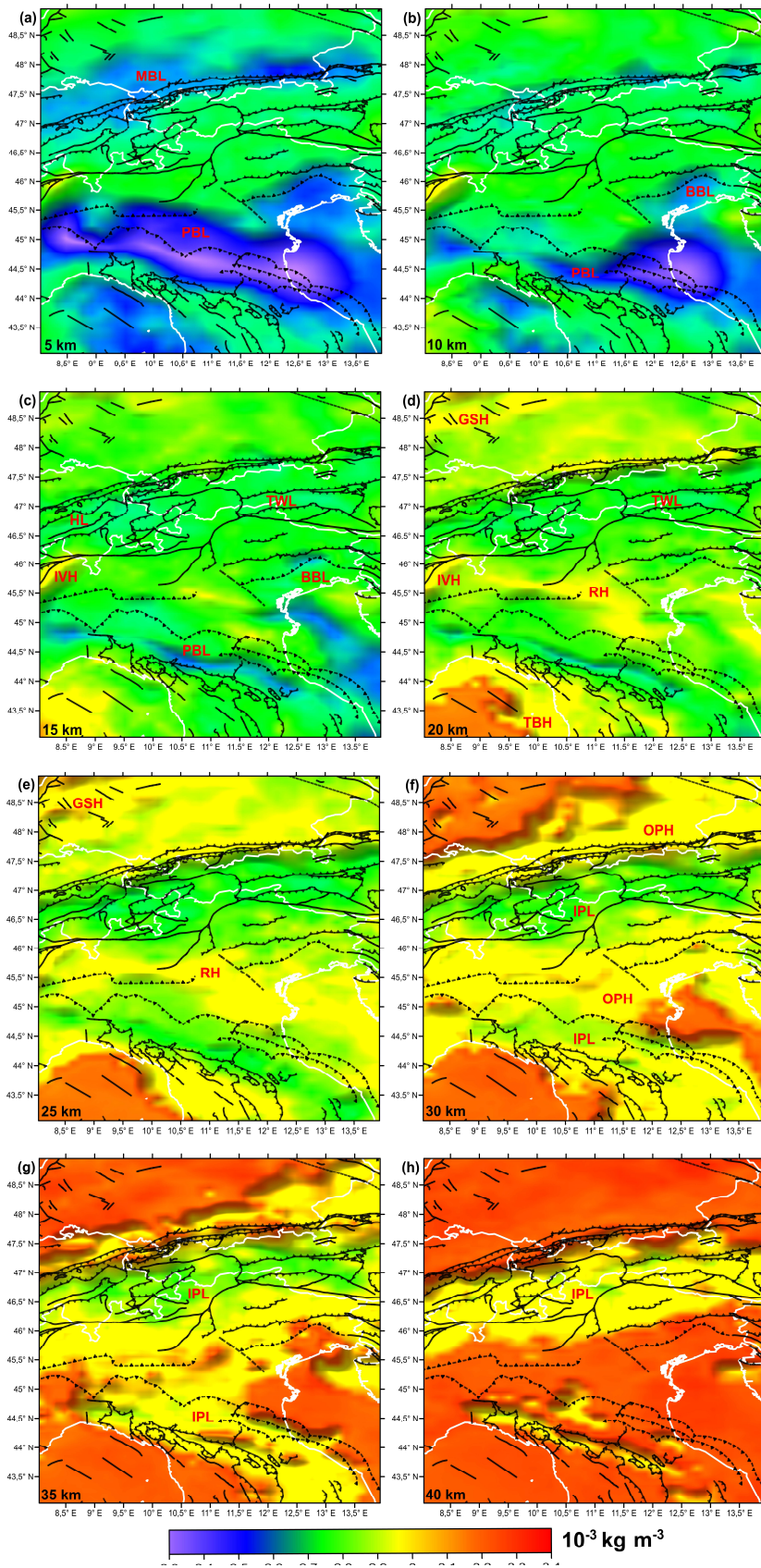


Figure 12 - Slice of density model, a)5km, b)10km, c)15km, d)20km, e)25km, f)30km, g)35km, h)40km. MBL: low density of Molasse basin; PBL: low density of Po basin; BBL: low density of Belluno basin; HL: low density of Helvetic nappe; TWL: low density of Tauern Window; IVH: high density of Ivrea-Verbano; GSH: high density of Rhine graben system; RH: high density values ridge; TBH: high density of Tyrrhenian basin; IPL: low density of orogen inner part; OPH: high density of orogen outer part.

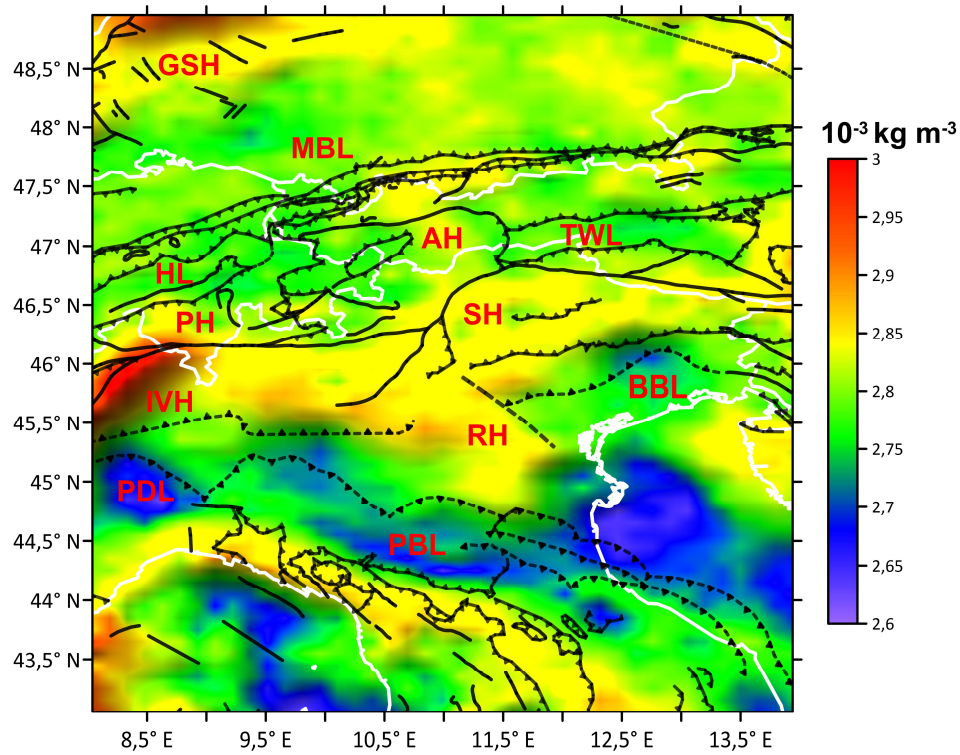


Figure 13 – Average density map; MBL: low density of Molasse basin; PBL: low density of Po basin; BBL: low density of Belluno basin; PDL: low density of Piedmont basin; HL: low density of Helvetic nappe ; PH: high density of Penninic Nappe; AH: high density of Austroalpine Nappe; TWL: low density of Tauern Window; IVH: high density of Ivrea-Verbano; GSH: high density of Rhine graben system; RH: high density values ridge; SH: high density of Southalpine.

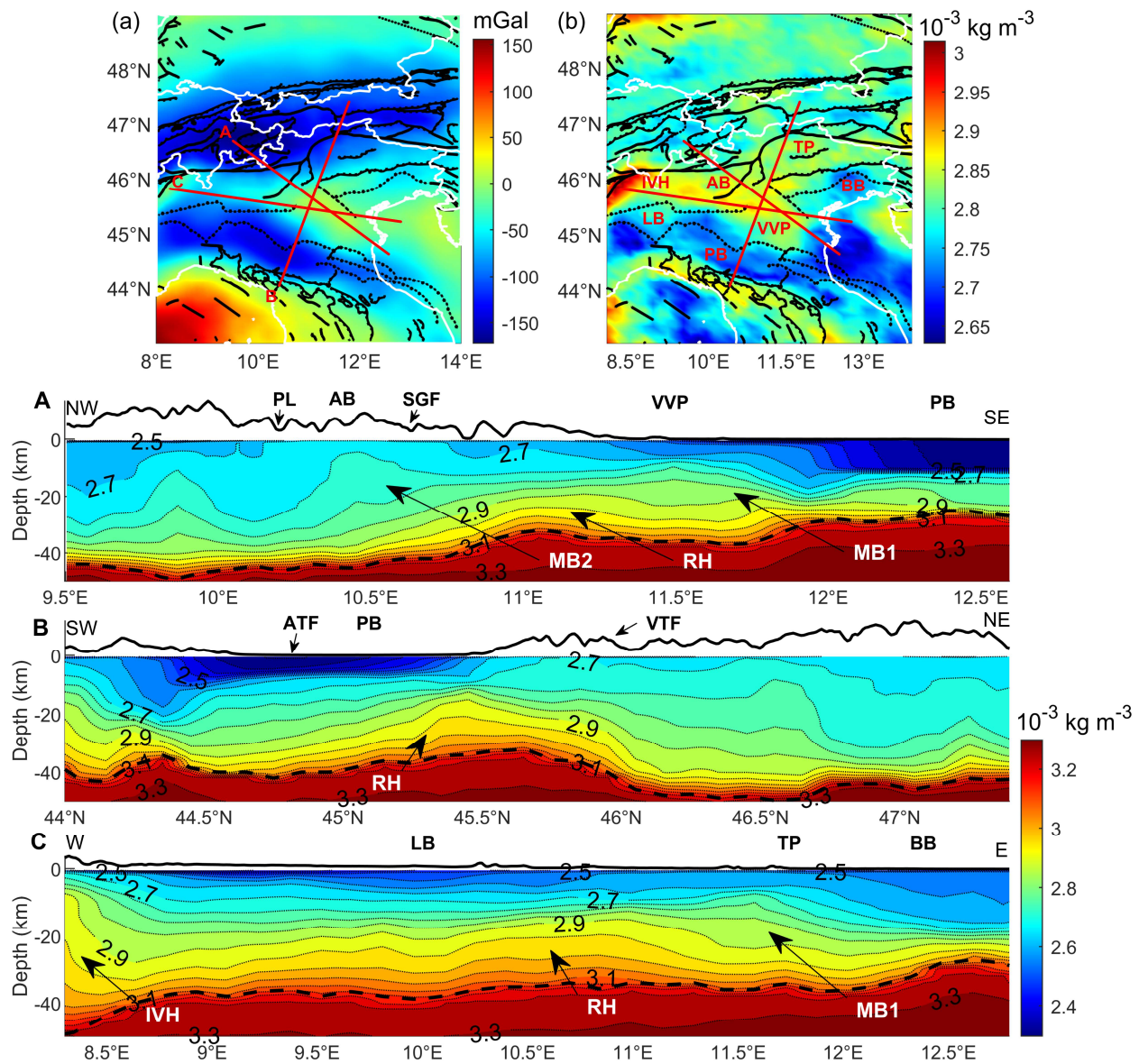


Figure 14 – Sections across the 3D density model for illustration. A) A section oriented NW-SE centered on the Vicenza-Verona gravity high. B) SW-NE oriented profile centered on the gravity high. C) Detailed profile oriented WNW-SSE centered on the gravity high; MB1: first mushroom shaped body with high density; MB2: second mushroom shaped body; PB: Po basin; VVP: Venetian Volcanic Province; SGF: South Giudicarie fault; AB: Adamello Batholith; PL: Periadriatic Line; VTF: Valsugana Thrust Front; ATF: Apennine Thrust Front; RH: High density Ridge; IVH: High density anomaly of Ivrea-Verbano; BB: Belluno Basin; TP: Trento Platform; LB: Lombardian basin.